# Mine Impact Burial Prediction From One to Three Dimensions

**Peter C. Chu**[1]
Naval Ocean Analysis and Prediction Laboratory,
Naval Postgraduate School,
Monterey, CA 93943
e-mail: pcchu@nps.edu

*The Navy's mine impact burial prediction model creates a time history of a cylindrical or a noncylindrical mine as it falls through air, water, and sediment. The output of the model is the predicted mine trajectory in air and water columns, burial depth/orientation in sediment, as well as height, area, and volume protruding. Model inputs consist of parameters of environment, mine characteristics, and initial release. This paper reviews near three decades' effort on model development from one to three dimensions: (1) one-dimensional models predict the vertical position of the mine's center of mass (COM) with the assumption of constant falling angle, (2) two-dimensional models predict the COM position in the $(x,z)$ plane and the rotation around the y-axis, and (3) three-dimensional models predict the COM position in the $(x,y,z)$ space and the rotation around the x-, y-, and z-axes. These models are verified using the data collected from mine impact burial experiments. The one-dimensional model only solves one momentum equation (in the z-direction). It cannot predict the mine trajectory and burial depth well. The two-dimensional model restricts the mine motion in the $(x,z)$ plane (which requires motionless for the environmental fluids) and uses incorrect drag coefficients and inaccurate sediment dynamics. The prediction errors are large in the mine trajectory and burial depth prediction (six to ten times larger than the observed depth in sand bottom of the Monterey Bay). The three-dimensional model predicts the trajectory and burial depth relatively well for cylindrical, near-cylindrical mines, and operational mines such as Manta and Rockan mines.* [DOI: 10.1115/1.3013823]

*Keywords: mine impact burial prediction, Kirchhoff–Kelvin equation, IBPM, IMPACT25/28, IMPACT35, drag and lift forces and torques, translation velocity, orientation, burial depth, sediment dynamics, triple coordinate system, mine shape effect, cylindrical mine, Manta mine, Rockan mine*

## 1 Introduction

In mine hunting, success often hinges on knowing as much as possible about the mines that have been placed and the environment that has affected the placement. Since bottom mines cannot be searched visually, and are often difficult to locate with conventional sonar, an estimate of area and height of the mine protruding from the sediment, or the burial depth, is crucial for the planning and execution of mine clearance operations. Determining the likely mine burial depth requires numerical models of the burial process and knowledge of the environment, including sediment properties, waves, tides, and water depth.

Sea deployed mines currently used by the United States and other nations fall into three general categories: bottom, moored, and drifting mines. Bottom mines rest on the ocean floor and are generally deployed in littoral regions. Common placements for bottom mines include shipping channels, harbors, anchorages, rivers, and estuaries. Bottom mines are deployed in one of the three ways: aircraft, surface ship, and submarine. Mine impact burial models have been developed to predict mine's motion in air and water and to determine the burial depth in sediment when the mine comes to rest in the sediment.

One-dimensional impact burial prediction model (IBPM) was developed by Arnone and Bowen [1] to predict the vertical position of the cylindrical mine's center of mass (COM) as it falls through air, water, and sediment. The burial depth of the mine in marine sediment is then calculated from the mine's velocity and the sediment characteristics. IBPM only solves the vertical momentum equation with the assumption of an unchanged orientation in the fluid.

Satkowiak [2,3] advanced Arnone and Bowen's [1] pioneering work through correcting reference flow for drag and added-mass calculations; reworking equations for sediment-cavity regime, drag due to the cylindrical and rounded noses, and resistant forces in semisolid sediment; and including water temperature effect on the water viscosity. The major weakness of the one-dimensional model is the mine's orientation (or the falling angle) assumed constant as it falls through the fluid.

Two-dimensional models were developed first by Hurst to overcome the major weakness of IBPM (constant falling angles) [4]. The models, written in BASIC (IMPACT25) and in MATLAB (IMPACT28), contain two momentum equations (in the $x$- and $z$-directions) and one moment-of-momentum equation (in the $y$-direction), include Mulhearn's [5] formulation for sediment bearing strength, and use multilayered sediments. They predict mine COM position in the $(x,z)$ plane and the rotation (i.e., mine orientation) around the $y$-axis.

Although the two-dimensional models advance our knowledge on the mine movement by including its rotation around the $y$-axis, it is very difficult to include the motion of the fluid. This is because it is hard to assume the fluid (air, water, and sediment) movement strictly in the $(x,z)$ plane. Any fluid motion in the $y$-direction induces drag force and in turn causes the mine movement (in the $y$-direction), which breaks the two-dimensional scenario [6,7]. In fact, it is impossible to lay a mine in the same vertical plane of the fluid velocity. Sensitivity studies on IMPACT25/28 burial depth show the insensitivity of the mine releasing height and the water temperature [8]. A mine drop experiment at Monterey Bay [9–11] shows that IMPACT25/28 overpredicts the burial depth.

Three-dimensional model (IMPACT35) has been developed with the support from the Office of Naval Research through Mine Burial Prediction Program [12–15]. The model contains three momentum equations and three moment-of-momentum equations. It

[1]Corresponding author.

Published online December 16, 2008. Transmitted by Assoc. Editor Firdaus E. Udwadia.

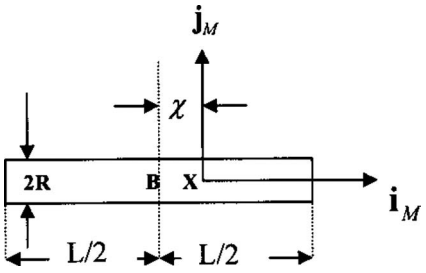


**Fig. 1** ***M*-coordinate with the COM as the origin of X and $(i_m, j_m)$ as the two axes. Here, $\chi$ is the distance between the COV (B) and Com (X), and $(L, R)$ are the cylinder's length and radius (after Chu et al. [13]).**

predicts the mine's COM position in the $(x,y,z)$ space and the rotation (i.e., mine's orientation) around the three axes. Several mine drop experiments conducted at the Naval Postgraduate School (NPS), Naval Undersea Warfare Center (NUWC)-Carderock, and Baltic Sea (by the German Navy) were used to evaluate the two- and three-dimensional models. The results show great improvement of the three-dimensional modeling.

The one-, two-, and three-dimensional models are reviewed in this paper. Basic physics, formulation, strength, and weakness of each model are presented. The purpose is to provide a overview of more than two decades' effort on predicting the mine (cylindrical and operational mine shape) movement in the air, water, and sediment column.

## 2 Mine Location and Orientation

Consider an axially symmetric cylinder with the COM **X** (or called gravity center (GC) in literatures) and the center of volume (COV) **B** on the main axis (Fig. 1). Let $(L,R,\chi)$ represent the cylinder length, the radius, and the distance between the two points $(\mathbf{X},\mathbf{B})$. The positive $\chi$-values refer to the nose-down case, i.e., point **X** is lower than point **B**. Let $F_E(O,\mathbf{i},\mathbf{j},\mathbf{k})$ be the earth-fixed coordinate (*E*-coordinate) with the origin *O*, and three axes: *x*-, *y*-axes (horizontal) with the unit vectors $(\mathbf{i},\mathbf{j})$ and *z*-axis (vertical) with the unit vector $\mathbf{k}$ (upward positive). The position of the cylinder is represented by the position of the COM,

$$\mathbf{X} = x\mathbf{i} + y\mathbf{j} + z\mathbf{k} \tag{1}$$

which is a translation of the cylinder. The translation velocity is given by

$$\frac{d\mathbf{X}}{dt} = \mathbf{V}, \quad \mathbf{V} = (u,v,w) \tag{2}$$

The orientation of the cylinder's main axis (pointing downward) is given by $\mathbf{i}_M$. The angle between $\mathbf{i}_M$ and $\mathbf{k}$ is denoted by $\psi_2 + \pi/2$ (Fig. 2). The angle $\psi_2$ is the mine falling angle. In the one- and two-dimensional modelings, only the *E*-coordinate system is used. In three-dimensional modeling, two extra-coordinate systems (main-axis following and force following coordinates) are also used.

## 3 Triple Coordinate Systems

Three coordinate systems are used in mine impact burial prediction modeling: earth-fixed coordinate (*E*-coordinate), main-axis following coordinate (*M*-coordinate), and force following coordinate (*F*-coordinate) systems. All the three coordinate systems are three dimensional, orthogonal, and right handed [16]. Projection of the mine's main-axis vector $\mathbf{i}_M$ onto the $(x,y)$ plane creates angle $(\psi_3)$ between the projection and the *x*-axis (Fig. 2). The *M*-coordinate is represented by $F_M(\mathbf{X},\mathbf{i}_M,\mathbf{j}_M,\mathbf{k}_M)$ with the origin **X** (i.e., the COM location), unit vectors $(\mathbf{i}_M,\mathbf{j}_M,\mathbf{k}_M)$, and coordinates $(x_M,y_M,z_M)$. The unit vectors of the *M*-coordinate system are given by

$$\mathbf{j}_M = \mathbf{k} \times \mathbf{i}_M, \quad \mathbf{k}_M = \mathbf{i}_M \times \mathbf{j}_M \tag{3}$$

The *M*-coordinate system is solely determined by orientation of the cylinder's main axis $\mathbf{i}_M$.

The *F*-coordinate is represented by $F_F(X,i_F,j_F,k_F)$ with the origin **X**, unit vectors $(\mathbf{i}_F,\mathbf{j}_F,\mathbf{k}_F)$, and coordinates $(x_F,y_F,z_F)$. Let $\mathbf{V}_w$ be the fluid velocity. The water-to-mine velocity is represented by

$$\mathbf{V}_r = \mathbf{V}_w - \mathbf{V} \tag{4}$$

which can be decomposed into two parts

$$\mathbf{V}_r = \mathbf{V}_1 + \mathbf{V}_2, \quad \mathbf{V}_1 = (\mathbf{V}_r \cdot \mathbf{i}_F)\mathbf{i}_F, \quad \mathbf{V}_2 = \mathbf{V}_r - (\mathbf{V}_r \cdot \mathbf{i}_F)\mathbf{i}_F \tag{5}$$

where $\mathbf{V}_1$ is the component paralleling to the cylinder's main axis (i.e., along $\mathbf{i}_M$), and $\mathbf{V}_2$ is the component perpendicular to the

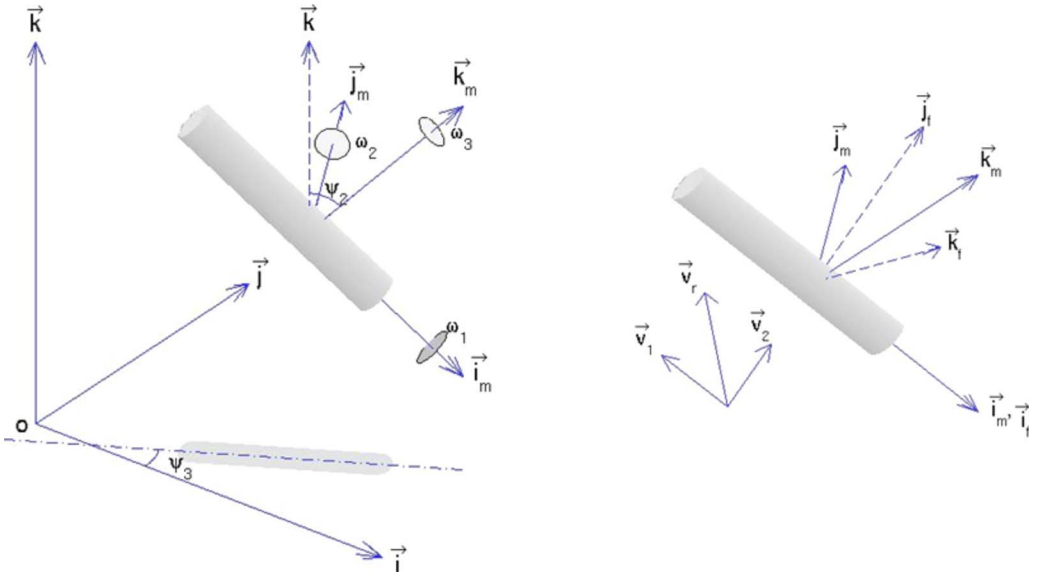


**Fig. 2 Mine's COM position $(x,z)$ and orientation $\psi_2$ (after Chu et al. [16])**

cylinder's main-axial direction. The unit vectors for the $F$-coordinate are defined by (column vectors)

$$\mathbf{i}_F = \mathbf{i}_M, \quad \mathbf{j}_F = \mathbf{V}_2/|\mathbf{V}_2|, \quad \mathbf{k}_F = \mathbf{i}_F \times \mathbf{j}_F \tag{6}$$

Transforms among the three coordinate systems can be found in Ref. [16].

## 4 One-Dimensional Modeling

One-dimensional models assume that the cylinder is not rotating (i.e., constant orientation) about any axis, nor a net fluid dynamic lift. Consequently, it can only be applied to stable motion of the body along one of its major axes (horizontal or vertical). The models predict the COM location (i.e., $z$) using the Kirchhoff–Kelvin theory. Only the $E$-coordinate system is used for the one-dimensional modeling.

**4.1 Kirchhoff–Kelvin Theory.** In the later half of the 19th century, Kirchhoff and Kelvin showed that the motion of a solid moving through an ideal fluid could be represented by a compact system of equations describing the coupled fluid-body dynamics [17,18]. Publications about the implications and extensions of this theory (cited as the Kirchhoff–Kelvin equations hereafter) were frequent from the 1870s until the 1900s, when experimental aerodynamics showed the limitations of the idealized models in representing the coupled dynamics of bodies and complex turbulent boundary layer regimes. Interest in the subject also waned due to the daunting nonlinearity of the governing equations. Recently there has been a resurgence of interest in the Kirchhoff–Kelvin theory, since the widespread availability of highly capable computers has allowed numerical analysis of problems involving nonlinear dynamics [19–21]. Even when analytical closure is not practical, the general results of the Kirchhoff–Kelvin equations aid heuristic explanations of the observed dynamics of more complex shapes, such as coins (very short cylinders) sinking in water [22] and tumbling cards [23]. In Ref. [24], excellent introductory can be found to the Kirchhoff–Kelvin equations and implications.

In general, the Kirchhoff–Kelvin equations predict the coupled dynamic response of arbitrary solid bodies to various forces and torques within inviscid incompressible flow. For high Reynolds number regimes ($\mathrm{Re}=UD/\nu > 10^4$, where $U$ is the velocity, $D$ is either the length or diameter of the cylinder depending on release orientation, and $\nu$ is the kinematic viscosity), the direct effect of viscosity is small such that coherent structures of the turbulent boundary layer diminish. The typical value of Re for mine falling through the water column is around $10^5$ [15]. This condition allows the generalized dynamics of falling bodies to be characterized in terms of a simplified form of the Kirchhoff–Kelvin theory where buoyancy force and turbulent drag are balanced by the inertia of the cylinder and displaced water. For a freely sinking cylinder of diameter $d$ and length $l$, the combined effect of buoyancy and gravity per unit volume is

$$B = -(\rho - \rho_w)g \tag{7}$$

where $g$ is the gravitational acceleration, and $(\rho - \rho_w)$ is the density difference of the cylinder and water. The flow over the cylinder surface yields pressure distributions that result in a net drag force ($F_d$) on the body, empirically represented as proportional to the square of the body's speed through water,

$$F_d \approx \tfrac{1}{2}\rho_w C_d U^2 \Lambda \tag{8}$$

where $C_d$ is the drag coefficient, $U$ is the mine's falling speed, and $\Lambda$ is an effective cross-sectional area normal to the flow. Under the assumption that the torques exerted by wake pressure fluctuations are insignificant, the phenomenological representation of the total drag force on the cylinder can be used in an approximation for the falling motion where the rate of change in kinetic energy is parametrized by the rate of change of the cylinder momentum and the acceleration of the "virtual mass" of the displaced water (which depends upon the geometric characteristics of the body). Thus, the force balance on the cylinder is given by

$$\frac{d^2z}{dt^2} = \frac{\rho_w C_d \Lambda}{2\rho\Pi(1+f)}\left(\frac{dz}{dt}\right)^2 - \frac{(\rho - \rho_w)}{\rho}g + \frac{F}{\rho\Pi} \tag{9}$$

where $\Pi$ is the volume of the mine, $f$ is the effective added-mass factor or the virtual mass coefficient of the system due to the acceleration of water around the moving body, and $F$ is the additional sediment force, which is zero in air and water. The left-hand side of Eq. (9) shows the vertical acceleration of the mine per unit mass. The right-hand side of Eq. (9) shows the external forces per unit mass exerted on the mine, with the first term from the drag force ($F_d$), the second term from the buoyancy force ($B$), and the third term from the sediment resistance.

Full implementation of the theory is not the focus of this work; however, stability analysis of particular variants of the Kirchhoff–Kelvin equation provides useful insights. We can characterize the generalized dynamics governing the motions of mines falling through water under the following hypothetical situations: vertical descent with the axis of the cylinder aligned parallel to the flow or vertical descent with the axis of the cylinder aligned perpendicular to the flow. For the simplest case where the axis of the cylinder is aligned with the fall direction, body motions will be stable unless they are significantly disturbed in a direction normal to the motion. This means that a vertically oriented cylinder dropped freely will maintain this orientation until external forces, such as variable turbulent drag, cause the motion to become unstable resulting in changes in orientation. With the axis of the cylinder oriented horizontally, or normal to the trajectory, the motion is also stable. An alternative scenario where the axis of the cylinder is not initially aligned either parallel or perpendicular to the flow makes the application of the above equations difficult but has been addressed in Ref. [25], who established that with time, the falling body will assume a horizontal orientation where the torque exerted on the body by the water turns the main axis of the cylinder, so that it is normal to the relative flow ("broadside"). This configuration is stable when the exposed area is normal to the flow and is significantly greater than the cross-sectional area of the "nose-on" attitude. Slight variations of this stable mode also exist including regular oscillations, glide tumble motions, and helical motions.

**4.2 IBPM.** The one-dimensional model is the first generation of the Navy's mine impact burial model [1–3], called the IBPM. This model is used to predict the vertical location and orientation of a cylindrical mine falling through air, water, and sediment through solving the Kirchhoff–Kelvin equation (9). The model consists of four major components: (a) steady falling attitude ($\psi_2$), (b) drag computation, (c) cavity regimes, and (d) sediment forces.

*4.2.1 Steady Falling Angle in Single Media.* IBPM does not use the moment-of-momentum equation for predicting mine orientation. Instead, the tangent of the falling angle (or called attitude) ($\psi_2$) is assumed as the ratio of moments due to the axial ($F_a$) and cross ($F_c$) forces [1]:

$$\tan\psi_2 = \frac{\mathrm{moment}(F_a)}{\mathrm{moment}(F_c)} \tag{10a}$$

where the axial and cross forces are calculated by

$$F_a = g(\rho - f_1\rho_w \sin^2\psi_2), \quad F_c = g(\rho - f_2\rho_w \cos^2\psi_2) \tag{10b}$$

Here, $(f_1, f_2)$ are the effective added-mass factors in the axial and cross mine directions,

$$f_1 = \frac{\alpha_0}{2-\alpha_0}, \quad f_2 = \frac{\beta_0}{2-\beta_0} \tag{11}$$

The two parameters $(\alpha_0, \beta_0)$ depend only on the aspect ratio ($\delta$),

$$\alpha_0 \equiv \frac{4}{\delta}\left(\frac{4}{\delta^2} - 1\right) - \left[\frac{1}{2}\ln\left(\frac{2+\delta}{2-\delta}\right) - \frac{\delta}{2}\right],$$

$$\beta_0 \equiv \frac{4}{\delta^2} - \frac{1}{\delta}\left(\frac{4}{\delta^2} - 1\right)\ln\left(\frac{2+\delta}{2-\delta}\right), \quad \delta \equiv \frac{2R}{L} \tag{12}$$

The effective added-mass factor is computed by

$$f = f_2 \sin\psi_2 + f_1 \cos\psi_2 \tag{13}$$

For an attitude $\psi_2$ of 0 deg (vertical), $f$ equals $f_1$. For an attitude $\psi_2$ of 90 deg (horizontal), $f$ equals $f_2$. In IBPM, the mine's attitude ($\psi_2$) is obtained by solving Eqs. (10*a*) and (10*b*) using the iteration method. Since the expression (10*b*) uses the fluid density ($\rho_w$), the mine's attitude ($\psi_2$) does not change in a single fluid but does change when it passes through the interface of two fluids. The effective cross-sectional area (or sometimes called projected area) $\Lambda$ depends on the attitude $\psi_2$,

$$\Lambda = 2LR\sin\psi_2 + \pi R^2 \cos\psi_2 \tag{14}$$

which is used for the drag calculation (see the next subsection). For an attitude of 0 deg (vertical), $\Lambda$ equals $\pi R^2$. For an attitude of 90 deg (horizontal), $\Lambda$ is the product of the length ($L$) and diameter ($2R$). It is noted that the physical base for "constant $\psi_2$ in a single fluid" is weak. This is because the mine's attitude ($\psi_2$) is determined by solving the moment-of-momentum equation (see Secs. 5.1 and 6.1) rather than solving Eqs. (10*a*) and (10*b*).

*4.2.2 Drag Coefficient*. Drag is caused by hydrodynamic forces acting on the falling cylinder in the axial and cross directions, and therefore it depends on the attitude ($\psi_2$) of the cylinder. The drag becomes somewhat more complicated because the feature of the flow across the cylinder changes based on the magnitude of the Reynolds number,

$$\mathrm{Re} = \frac{2UR}{\nu} \tag{15}$$

where $\nu$ is the kinematic viscosity of the fluid. When the Reynolds number is small ($<1$), skin friction dominates but as the Reynolds number increases, a more laminar flow occurs and the pressure drag dominates. At a certain and critical Reynolds number ($10^4$), flow becomes turbulent and drag abruptly decreases. Reynolds number is thus dependent on velocity of the cylinder and must be constantly recalculated as the cylinder falls through each medium.

Dependence of drag on (Re, $\psi_2$) is shown in the axial and cross drag coefficients ($C_{da}, C_{dc}$) [1]

$$C_{dc} = 1.1\,\eta C_{d\infty}\sin^2\psi_2, \quad C_{da} = 1.1 C_{d*}\frac{\Lambda}{2RL} \tag{16}$$

where

$$C_{d\infty} = \begin{cases} 0.84864 + 5.81939/\mathrm{Re} & \text{if } \mathrm{Re} \le 4\times 10^3 \\ (0.5833\times 10^{-4})\mathrm{Re} + 0.61677 & \text{if } 4\times 10^3 < \mathrm{Re} \le 10^4 \\ 1.2 & \text{if } 10^4 < \mathrm{Re} \le 8\times 10^4 \\ 1.19381 + (0.65828\times 10^{-6})\mathrm{Re} - 10^{-11}\,\mathrm{Re}^2 & \text{if } 8\times 10^4 < \mathrm{Re} \le 5\times 10^5 \\ 8\times 10^{-7}\,\mathrm{Re} - 0.15 & \text{if } \mathrm{Re} \ge 5\times 10^5 \end{cases} \tag{17}$$

is the cross flow drag coefficient for the cylinder with infinite length ($C_{d\infty}$), and

$$C_{d*} = 0.33\delta + \frac{3.984}{\sqrt{\mathrm{Re}}}\left[\frac{1}{\delta} + \delta^{1/2}\right] \tag{18}$$

is the axial drag coefficient with no surface imperfections. The coefficient of 1.1 in Eq. (16) is used to account for imperfections of the cylinder with the correction factor $\eta$ given by

$$\eta = 0.52238 + 0.02119\frac{1}{\delta} - 0.00048\left(\frac{1}{\delta}\right)^2 \tag{19}$$

The total drag coefficient ($C_d$) for computing the drag force on a mine moving through the fluid is calculated by

$$C_d = C_{da} + C_{dc}\sin^2\psi_2 \tag{20}$$

*4.2.3 Air-Water Cavity*. Upon impacting the water, the cylindrical mine enters the air-water cavity. The properties of the fluid in the water cavity are combination of air and water fluid properties and are continuously changing with time. It is extremely difficult to accurately predict the forces acting on a body in a fluid of changing properties [1,26]. The changing properties around the cylinder through the cavity are the fluid density and kinematic viscosity. For example, the fluid density changes from air ($\rho_a = 1.29\ \mathrm{kg\,m^{-3}}$) to sea water ($\rho_w = 1025\ \mathrm{kg\,m^{-3}}$).

Within the air-water cavity regime, a percentage of each of these densities is used in determination of the resulting average density. This is represented by the ratio (called the void ratio) of the volume of water in the cavity to the total cavity volume. Although it is difficult to actually determine these volumes, the trend of this ratio is known. For example, the void ratio equals "0" for the cylinder in the air and equals "1" for the cylinder totally wetted in the water.

When the pressure generated by the dynamic loading of the cylinder impacting on the water is balanced by the hydrostatic pressure of the water. The air-water cavity is assumed to collapse and the cylinder is fully wetted. The dynamic pressure generated by the cylinder ($p_D$) is the sum of the atmospheric pressure $p_a$ (=100 kPa) at the water surface and dynamic pressure due to the cylinder's falling velocity $U$,

$$p_D(t) = p_a + \tfrac{1}{2}\rho_w[U(t)]^2 \tag{21a}$$

The hydrostatic pressure ($p_S$) of water is the sum of the atmospheric pressure ($p_a$) and weight of the water column,

$$p_S(t) = p_a - \rho_w g z(t) \tag{21b}$$

In the IBPM, the square root of the ratio between $p_D$ and $p_S$ is defined as the void ratio $n_0$

$$n_0(t) = \sqrt{\frac{p_D(t)}{p_S(t)}} \tag{22}$$

which is taken as a weight of water in the air-water cavity. The cavity density ($\rho_w^{\mathrm{cav}}$) and viscosity ($\nu_w^{\mathrm{cav}}$) are calculated by

$$\rho_w^{\mathrm{cav}} = \rho_a(1-n_0) + \rho_w n_0, \quad \frac{1}{\rho_w^{\mathrm{cav}}\nu_w^{\mathrm{cav}}} = \frac{(1-n_0)}{\rho_a\nu_a} + \frac{n_0}{\rho_w\nu_w} \tag{23}$$

The dynamic effect of cavitation on the body is through the change of the Reynolds number (in turn the change of the drag coefficient). The Reynolds number for the air-water cavity is calculated by

$$\mathrm{Re}_w^{\mathrm{cav}} = \frac{2UR}{\nu_w^{\mathrm{cav}}}$$

Substitution of $\mathrm{Re}_w^{\mathrm{cav}}$ into Eqs. (16)–(20) leads to the drag coefficient for the air-water cavity.

*4.2.4 Water-Sediment Cavity*. Upon impacting the sediment, the cylindrical mine creates a cavity in which the fluid properties of water and sediment are interacting. Similar to the air-water cavity regime, the properties of the water-sediment cavity are combination of water and sediment properties and are continuously changing with time. In the water-sediment cavity regime, the fluid density changes from water ($\rho_w = 1025\ \mathrm{kg\ m^{-3}}$) to sediment $\rho_s$. Within the water-sediment cavity, the void ratio $n_1$

$$n_1(t) = \sqrt{\frac{p_D(t)}{p_S(t)}} \tag{24}$$

is taken as the weight of the sediment in water-sediment cavity. Here,

$$p_D(t) = p_a + \rho_w g h + \tfrac{1}{2}\rho_s[U(t)]^2, \quad p_S(t) = p_a + \rho_w g h - \rho_s g[z(t) + h] \tag{25}$$

are the dynamic and static pressures, and $h$ is the water depth. The water-sediment cavity density ($\rho_s^{\mathrm{cav}}$) and viscosity ($\nu_s^{\mathrm{cav}}$) are calculated by

$$\rho_s^{\mathrm{cav}} = \rho_w(1 - n_1) + \rho_s n_1, \quad \frac{1}{\rho_s^{\mathrm{cav}}\nu_s^{\mathrm{cav}}} = \frac{(1 - n_1)}{\rho_w \nu_w} + \frac{n_1}{\rho_s \nu_s} \tag{26}$$

The kinematic viscosity of the sediment is determined by

$$\nu_s = \nu_w + \frac{S}{\rho_s dU/dz} \tag{27}$$

where $S$ is the shear strength of the sediment. Substitution of $\nu_s$ into Eq. (15) leads to a new Reynolds number; and then use of Eqs. (16)–(20) leads to the drag coefficient for the water-sediment cavity.

*4.2.5 Sediment Forces*. Forces exerting on mine in sediment are different from that in air and water, especially the sediment resistant force ($F$), which is calculated in IBPM using two different methods. The first method [1] is velocity independent. It decomposes the sediment resistant force into compressive force ($F_C$) and shearing force ($F_S$),

$$F = F_C + F_S \tag{28a}$$

where $(F_C, F_S)$ are proportional to the shear strength ($S$) with the proportionalities of the cylindrical reference flow areas $(\Lambda_f, \Lambda_s)$ in the front (twice) and in the side (once),

$$F_C = 2S\Lambda_f, \quad F_S = S\Lambda_s \tag{28b}$$

The second method is velocity dependent [3]. The sediment resistant force is calculated by

$$F = E_s S(N_b \Lambda_f + S_{\mathrm{af}}\Lambda_s/S_t) \tag{29}$$

where $E_s$ is the sediment strain rate (i.e., ratio of the sediment strength for a given velocity of the cylinder), $N_b$ (=10) is the bearing capacity factor, $S_{\mathrm{af}}$ is the side adhesive factor (0.3 for the cavity and 1.0 for sediment), and $S_t$ (=3) is the sediment sensitivity coefficient.

Thus, the sediment shear strength and density data are the inputs to the Kirchhoff–Kelvin equation (9) for mine movement in the sediment since they are needed for determination of the sediment's compressive and shearing forces, buoyancy force, added mass, drag force, and kinematic viscosity. Since the properties of sediment change with depth, the sediment density and shear strength profiles with 5 cm vertical resolution are used in the IBPM.

**4.3 Sensitivity Studies.** For a single medium, after the attitude ($\psi_2$) is determined from Eq. (10*a*) and (10*b*), the effective cross-sectional area $\Lambda$ and the effective added-mass factor $f$ can be calculated using Eqs. (11) and (12), and then the total drag coefficient $C_d$ can be computed using Eq. (20). For sediment, the compressive and shear stress forces $(F_C, F_S)$ are computed from the density and shear strength. With the known parameters ($\Lambda$, $f$, $C_d$, $F_C$, and $F_S$), the Kirchhoff–Kelvin equation (9) can be solved for mine movement. For mine penetration into the air-water and water-sediment interfaces, the total drag coefficient $C_d^{\mathrm{cav}}$ is calculated from the cavity density ($\rho_w^{\mathrm{cav}}$ or $\rho_s^{\mathrm{cav}}$) and viscosity ($\nu_w^{\mathrm{cav}}$ or $\nu_s^{\mathrm{cav}}$).

Arnone and Bowen [1] conducted a model sensitivity study on the mine air weight (or wet weight), length, and radius. The model (9) was integrated with various combinations of these parameters and three different attitudes: $\psi_2 = 0$ deg, (horizontal), 45 deg, and 90 deg (vertical). The water impact velocity has the following features. (a) For mine movement in the air, as one would expect, the more streamlined the falling attitude (i.e., $\psi_2 = 90$ deg vertical), the higher velocity the cylindrical mine falls. (b) The water impact velocity varies drastically with the attitude for light mines. Such an effect reduces as the mass increases. (c) The water impact velocity is not sensitive to mine length ($L$) and radius ($R$).

The mine falling velocity in the water has the following characteristics. (a) It varies drastically with attitude and wet weight. For the same wet weight, the mine falls faster for $\psi_2 = 90$ deg (vertical) than for $\psi_2 = 0$ deg (horizontal). For the same $\psi_2$, the mine falls faster for heavier wet weight. (b) It is not sensitive to attitude for short mines and is very sensitive to attitude for long mines. (c) It is not sensitive to mine length for horizontal release ($\psi_2 = 0$ deg) and is very sensitive to mine length for vertical release ($\psi_2 = 90$ deg). (d) It is not sensitive to attitude for small $R$ and is very sensitive to attitude for large $R$. (e) It is not sensitive to attitude for small $R$ and is very sensitive to attitude for large $R$.

**4.4 Strength and Weakness.** IBPM has capability to simulate mine falling velocity in the air and water columns. As mentioned in the previous subsection, the model provides the following useful results: (a) The mine has higher falling velocity for vertical release ($\psi_2 = 90$ deg) than for the horizontal release ($\psi_2 = 0$ deg), (b) the water impact velocity varies drastically with the attitude for light mines but does not for heavy mines, and (c) the mine falling velocity in water column is sensitive to attitude, wet weight, mine length, and mine radius. For the same mine, the falling velocity in water is minimum for horizontal orientation and maximum for vertical orientation.

Weakness of the IBPM is to assume the constant attitude ($\psi_2$) during the mine falling through a single medium (air, water, or sediment) (Fig. 3), which is physically unrealistic [12]. In fact, the orientation changes for any solid object falling through fluid (air and water). When COV is not colocated with COM, the buoyancy force (**B**) has a moment of momentum exerted on mine (Fig. 4) [27]. If the mine slants toward left (right), the moment of momentum due to the buoyancy force will rotate the mine clockwise (anticlockwise). This causes the spiral motion for mine falling through fluid.

## 5 Two-Dimensional Modeling

To overcome the major weakness of the one-dimensional model (i.e., constant attitude $\psi_2$), Hurst [4] modified the IBPM model through allowing the cylinder to move both vertically and horizontally (in the $(x, z)$ plane) as well as rotation about the $y$-axis.

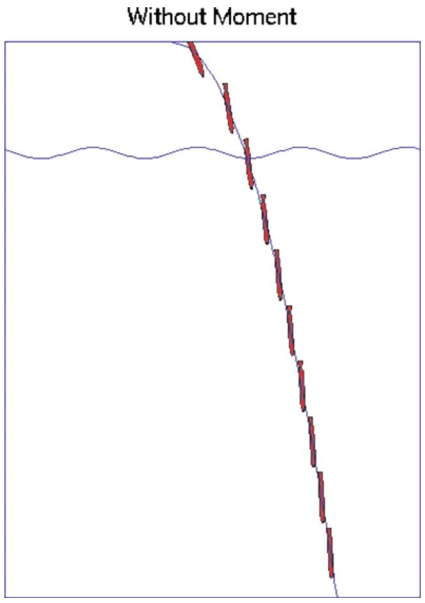


**Fig. 3 Mine's orientation is assumed constant by the one-dimensional model when it falls through a single fluid (after Chu [12])**

These changes mandated the use of more complicated dynamical system than the IBPM. Two coordinate systems ($E$- and $M$-coordinates) are used in the two-dimensional models.

**5.1 Dynamical System.** Let the cylinder be moving in the $(x,z)$ plane. The momentum equations in the $(x,z)$ directions are given by

$$\frac{d^2x}{dt^2} \equiv \frac{du}{dt} = \frac{F_h^x}{\rho\Pi} \tag{30}$$

$$\frac{d^2z}{dt^2} \equiv \frac{dw}{dt} = -g + \frac{B + F_h^z}{\rho\Pi} \tag{31}$$

where $B$ is the buoyancy force, and $(F_h^x, F_h^z)$ are the components of the hydrodynamic force $\mathbf{F}_h$. Since the cylinder is restricted in the $(x,z)$ plane, the only possible rotation is around the $y$-axis, which is described by the attitude $\psi_2$. The moment-of-momentum equation is written in the $M$-coordinate system,

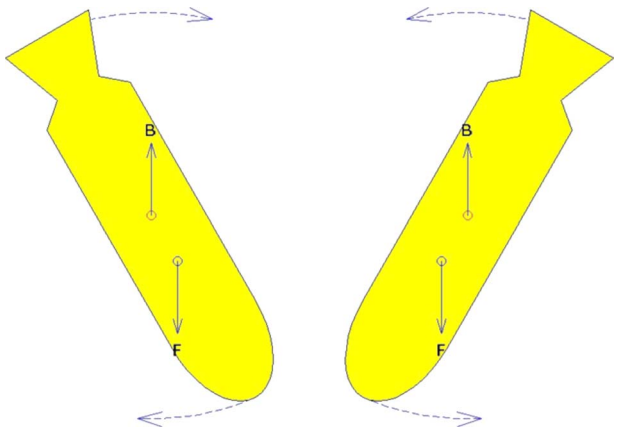


**Fig. 4 Change of mine orientation caused by momentum due to the buoyancy force (after Chu [27])**

$$J_2\frac{d^2\psi_2}{dt^2} = B\chi\cos\psi_2 + M_h^y \tag{32}$$

where $J_2$ is the moment of inertia in the $y$-axis, and $M_h^y$ is called the braking torque in Ref. [4].

**5.2 IMPACT25/28.** The two-dimensional models, usually called IMPACT25 (written in BASIC) and IMPACT28 (written in MATLAB), are the second generation of the Navy's mine impact burial prediction models for cylindrical mines and were based on Eqs. (30)–(32) for obtaining $(x,z,\psi_2)$. The external forcing for IMPACT25/28 consists of drag force $(F_h^x, F_h^z)$ and braking torque $(M_h^y)$. Since the mine movement is restricted in the $(x,z)$ plane, it is very hard to include the motion of the fluids (air or water). If the fluid has velocity in the $y$-direction, the mine's motion cannot be two dimensional. Thus, in IMPACT25 and IMPACT28, the fluid (air or water) is assumed motionless.

*5.2.1 Drag Force*. The drag force for the whole cylinder is calculated in two directions: along the cylinder's main axis $(\mathbf{i}_M)$ and across the cylinder $(\mathbf{k}_M)$,

$$\mathbf{F}_d = -F_d(\mathbf{i}_M\sin\psi_2 - \mathbf{k}_M\cos\psi_2) \tag{33}$$

where $F_d$ is computed using the drag law

$$F_d = \tfrac{1}{2}\rho_w\hat{C}_d(u^2 + w^2)\Lambda \tag{34}$$

The drag coefficient $\hat{C}_d$ is computed by

$$\hat{C}_d = C_d + C_{dn} \tag{35}$$

where $C_d$ is computed in the same way as in the one-dimensional model (i.e., Eq. (20)), and $C_{dn}$ is the drag coefficient for the nose.

*5.2.2 Braking Torque*. The braking torque $M_h^y$ in Eq. (32) is calculated by

$$M_h^y = -\tfrac{1}{6}C_{dc}R\rho_w\omega_2L^3V_c \tag{36}$$

where

$$V_c = u\cos\psi_2 + w\sin\psi_2 \tag{37}$$

is the cross-cylinder velocity. Equation (36) is only used when the mine is fully immersed in a single fluid. During the cavity regimes, a different calculation is applied. Furthermore, the torque is in opposite sign to rotation and thus acts as the brake to the rotation of mine. For a single fluid, the basic equations (30)–(32) are integrated in association with Eqs. (33) and (36).

*5.2.3 Sediment*. The one-dimensional models (IPBM and its modifications) treat sediment as fluid with two characterized parameters: sediment density and shear strength. Different from the one-dimensional models, the two-dimensional models treat the sediment as solid that undergoes plastic deformation [4]. The pertinent parameters are sediment density and bearing strength. The bearing strength is the load bearing capacity of the sediment and defined as the pressure in front of the object penetrating the sediment. It is related to the shear strength, typically larger by a factor of about 10. Three elements contributing to the sediment resistance on the penetration of a falling mine are included in IMPACT25/28: bearing strength of the sediment (70%), hydrodynamic drag (25%), and buoyancy (5%) [4].

As the mine penetrates the sediment, the hydrodynamic drag that retards the penetration is calculated by

$$F_d = \frac{\rho_s\Lambda(u^2 + w^2)}{2}\left(C_1\frac{h}{L} + C_2\right) \tag{38}$$

where $C_1$ and $C_2$ are the drag coefficients for low Reynolds number and $h$ is the depth in sediment. The buoyancy force comes into play when the mine impacts the sediment. A crater is formed and

the force that is required to create and enlarge the crater is given by Eq. (4)

$$B = \pi g h(\rho_w - \rho)\Lambda \tag{39}$$

Two assumptions are made regarding the mine. First, the buoyancy force acts uniformly on the portion of the mine in contact with the sediment. Second, a cavity is formed, remains at the aft end of the mine, and leads the mine surface to the buoyancy force. The second assumption is not always true. For some cases, the cavity collapses under the weight of the sediment. The collapse limit is defined and approximated as the depth where the buoyancy force is 20% of the bearing force. Besides, the drag, buoyancy, and bearing strength of sediment all depend on the mine contact area $\Lambda$.

*5.2.4 Air-Water Cavity*. As mentioned before, when the mine penetrates the air-water interface, it forms a cavity behind the mine that changes the drag forces. Throughout the cavity regimes, nonsymmetric forces are acting on the mine that generate torque and affect the rate of rotation. The cavity parametrization is different between the two-dimensional models (IMPACT25/28) and one-dimensional model (IPBM). The cavity formation in the two-dimensional models is controlled by the cavitation number ($N_{\text{cav}}$) defined by

$$N_{\text{cav}} = \frac{2(p_{\text{out}} - p_{\text{in}})}{\rho_w(u^2 + w^2)} \tag{40}$$

where ($p_{\text{out}}, p_{\text{in}}$) are the hydrodynamic pressure outside (i.e., water) and inside the cavity. Pressure difference between the outside and inside of the cavity increases or the mine's velocity decreases; the cavitation number increases until the eventual collapse of the cavity. The drag coefficient of the cavity is the function of the cavitation number,

$$C_d(N_{\text{cav}}) = \hat{C}_d(1 + bN_{\text{cav}}) \tag{41}$$

When the air-water cavity collapses, $N_{\text{cav}}=0$, $C_d(0)$ is the water drag coefficient. The torque in the air-water cavity can be computed after the drag coefficient is determined.

**5.3 Sensitivity Study.** Sensitivity studies [8,28] were conducted on the two-dimensional model (IMPACT25/28) to ascertain which parameters the model is most sensitive to and which can be eliminated in order to simplify its use. The model was altered to allow most parameters to be set and a loop run for one variable at a time. All model runs were made with preset mine profile, which has a dry weight of 538 kg, a wet weight of 251 kg, and a uniform diameter of 0.475 m.

*5.3.1 Sensitivity to Release Parameters*. Figure 5 demonstrates the sensitivity of the release altitude and other model parameters such as water depth and water temperature. Altitude, when varied from 0 m to 1000 m, has a small effect on burial depth (relative difference of 18%). When a more realistic upper limit of 300 m for a mine laying aircraft is applied, the relative difference drops to 9%. Water depth affects the burial depth only if a mine reaches the terminal velocity (in this case about 20 m). Although temperature varies the water density up to 3% and in turn changes the viscosity [29], it does not affect the burial depth and orientation.

For vertical initial falling angle (Fig. 6) with zero rotation rate, the mine is heading directly downward, resulting in the maximum burial depth. When the release height is 150 m, the mine burial depth is 2.405 m for the vertical initial falling angle and 0.359 m for the horizontal initial falling angle. Such a difference in burial depth decreases as the release height decreases. When the release height is 1.5 m, the mine burial depth is 0.977 m for the vertical initial falling angle and 0.342 m for the horizontal initial falling angle.

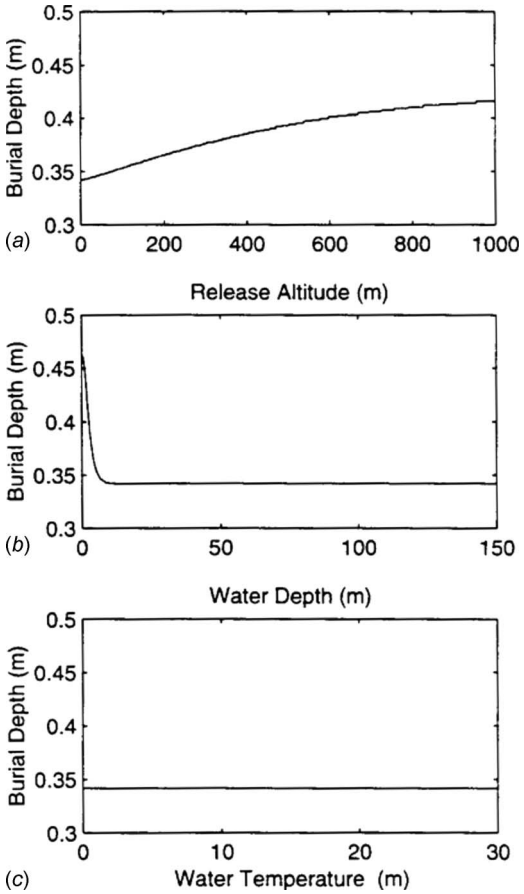


**Fig. 5 Effect of (*a*) release attitude, (*b*) water depth, and (*c*) water temperature on burial depth. Values are primarily chosen to represent all conditions under which IMPACT25 and IMPACT28 may be used (after Chu et al. [28]).**

*5.3.2 Sensitivity to Sediment Characteristics*. Figure 7 shows the sensitivity of sediment density and shear strength on burial depth. For the shear strength of 1 kPa (extremely soft sediment), the burial depth decreases 37% for sediment density varying from 1000 kg/m$^3$ to 2000 kg/m$^3$. For more commonly used values of shear strength (5–15 kPa), the sediment density has very little effect, just 3.7% (Fig. 7(*a*)). As shear strength increases, the influence of sediment density reduces. For constant sediment density (1.5 kg m$^{-3}$), the impact burial depth drastically reduces from 0.55 m for the shear strength of 1 kPa to 0.1 m for the shear strength of 10 kPa (Fig. 7(*b*)).

A power law is used

$$S = \alpha \rho_s^{\beta} \tag{42}$$

to represent the relationship between sediment density ($\rho_s$) and shear strength ($S$) [30]. Here the two coefficients $\alpha$ and $\beta$ are determined experimentally. Considering a homogeneous sediment layer ($\rho_s$=const), the shear strength is a function of ($\alpha, \beta$). For a given $\rho_s$, increasing $\alpha$ or $\beta$ enhances the shear strength ($S$) and in turn decreases the burial depth. These features are well simulated by the model (Fig. 8).

**5.4 Strength and Weakness.** The improvement of the two-dimensional model versus the one-dimensional model is its capability to predict the mine rotation in the ($x, z$) plane, i.e., $\psi_2$. In the two-dimensional model, the momentum equation for the ($x, z$) directions and the moment-of-momentum equation for the $y$-direction are used to predict the position and orientation around

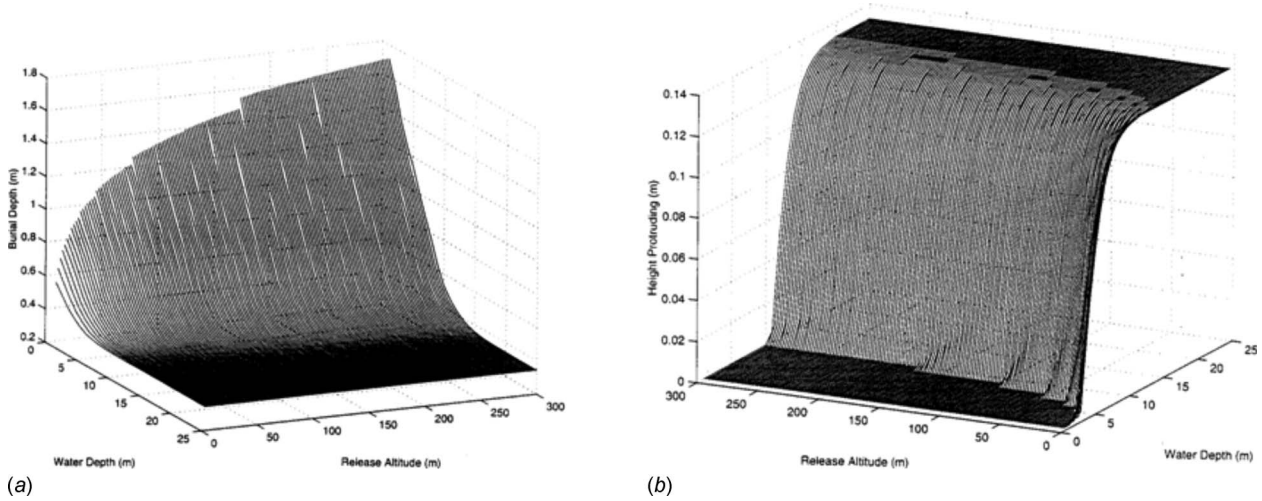


(*a*) (*b*)

**Fig. 6 Dependence of (*a*) burial depth (m) and (*b*) height protruding (m) on release altitude (m) and water depth (m). Height protruded is illustrated here to clarify the levels at which these parameters become less influential in the two-dimensional models (after Chu et al. [28]).**

the $y$-axis (i.e., in the $(x,z)$ plane). The basic physics for the spiral motion described in Fig. 4 is included in the two-dimensional model but strictly in the $(x,z)$ plane [31,32].

Since the mine movement is strictly in the $(x,z)$ plane, it is very hard to include the motion of fluid in the two-dimensional model because it is impossible to lay a mine in the same direction of the fluid velocity. In the littoral zone, the water velocity is not negligible. The application of the two-dimensional model for the operational use is limited. Besides, the drag coefficients for the axial and cross directions have similar dependence on the Reynolds number Re and the aspect ratio ($\delta$) (see Eqs. (17) and (18)). However, the drag coefficients in the axial and cross directions are independent [33]. Besides, a mine drop experiment shows that IMPACT25/28 overpredicts (five to ten times larger) the mine

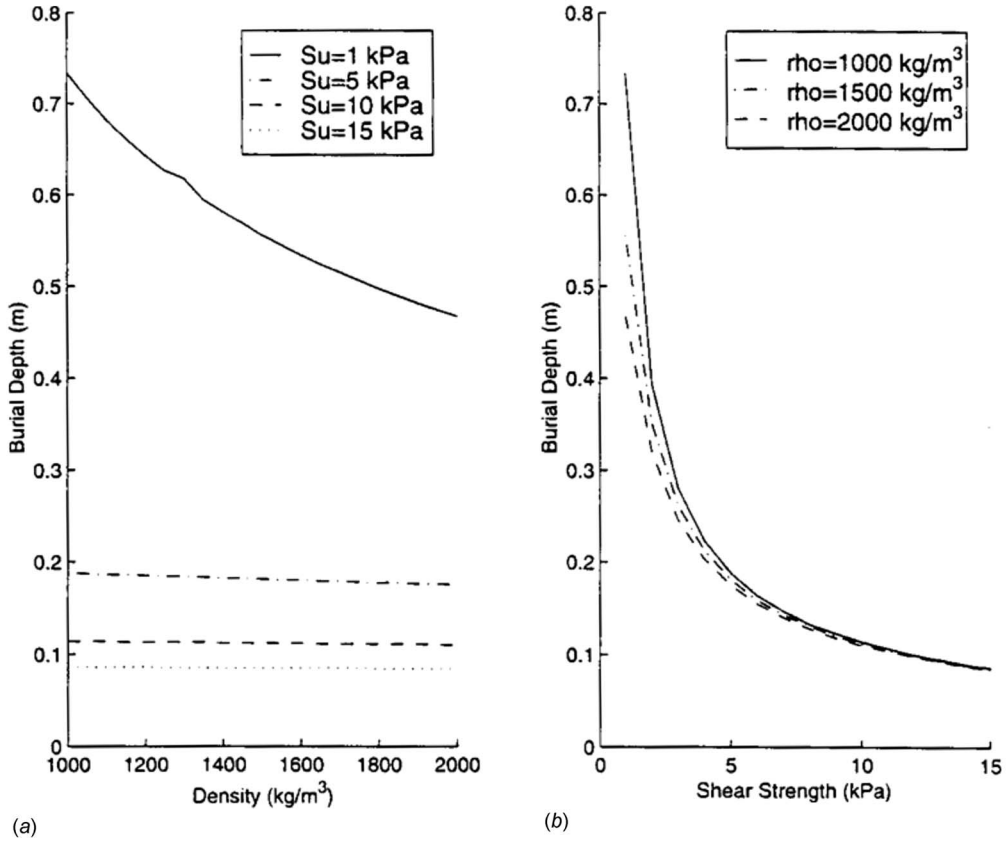


(*a*) (*b*)

**Fig. 7 Effect of sediment (*a*) density and (*b*) shear strength on burial depth. Density change only impacts the predicted burial depth in very soft sediments. As expected, shear strength has a dramatic impact on predicted burial depth (after Chu et al. [31])**

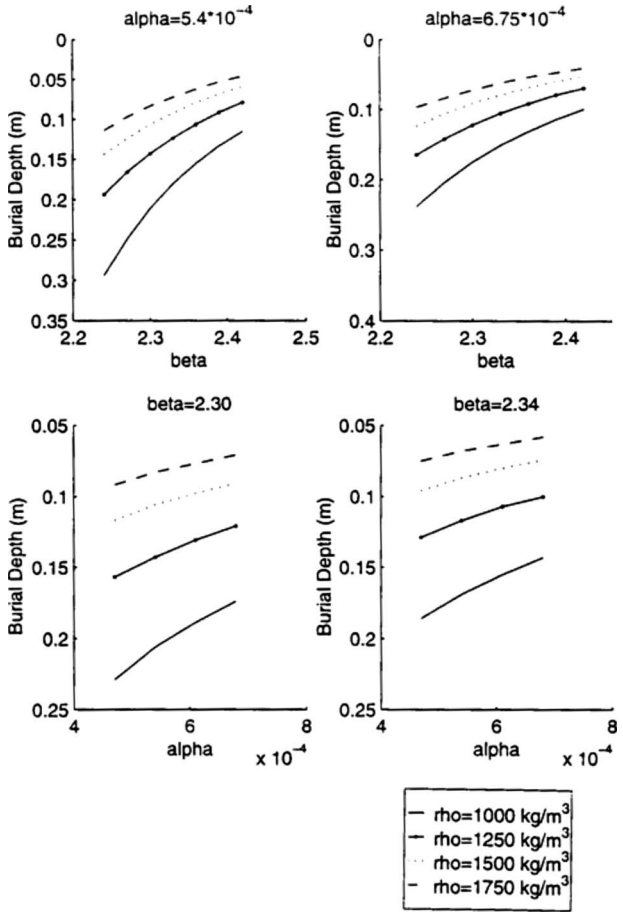


**Fig. 8 Effect of $\alpha$ and $\beta$ on predicted burial depth (m) for different values of sedimentary density (after Chu et al. [31])**

burial in the sandy bottom [9,31,32]. This indicates that the sediment dynamics is too simple in the two-dimensional model.

## 6 Three-Dimensional Modeling for Cylindrical Mines

To overcome the major weaknesses of the two-dimensional model, i.e., (a) environmental fluid assumed motionless, (b) similar drag coefficients in the axial and cross directions, and (c) nonrealistic sediment dynamics, Chu et al. [10–16,34–38] modified IMPACT25/28 allowing the cylinder to move in three-dimensional space. These changes mandated the use of more complicated dynamical system than IMPACT25/28. The three coordinate systems (*E*-, *F*-, and *M*-coordinates) are used in the three-dimensional modeling.

**6.1 Dynamical System.** The three momentum equations (in the *E*-coordinate system) are given by

$$\frac{d}{dt}\begin{bmatrix} u \\ v \\ w \end{bmatrix} = -\begin{bmatrix} 0 \\ 0 \\ g \end{bmatrix} + \frac{\mathbf{F}_b + \mathbf{F}_h}{\rho \Pi} \tag{43}$$

and the three moment-of-momentum equations (in the *M*-coordinate system) are written in vector form

$$\mathbf{J} \cdot \frac{d\boldsymbol{\omega}}{dt} = -2\mathbf{J} \cdot (\boldsymbol{\Omega} \times \boldsymbol{\omega}) + \mathbf{M}_b + \mathbf{M}_h \tag{44}$$

Here, $(\mathbf{F}_b, \mathbf{M}_b)$ are the buoyancy force and torque, and $(\mathbf{F}_h, \mathbf{M}_h)$ are the hydrodynamic force and torque including the drag, lift, and impact $(\mathbf{F}_d, \mathbf{F}_l, \mathbf{F}_i; \mathbf{M}_d, \mathbf{M}_l, \mathbf{M}_i)$. The vectors $(\boldsymbol{\omega}, \boldsymbol{\Omega})$ are the angular velocity of mine and *M*-coordinate system,

$$\boldsymbol{\Omega} = \omega_2 \mathbf{j}_M + \omega_3 \mathbf{k}_M \tag{45}$$

The first term in the right-hand side of Eq. (44) is an apparent torque (similar to the Coriolis term in earth science) due to the use of the rotating coordinate system (i.e., the *M*-coordinate). If $\omega_1 = 0$, then $\boldsymbol{\Omega} = \boldsymbol{\omega}$. The apparent torque is given by

$$-2\mathbf{J} \cdot (\boldsymbol{\Omega} \times \boldsymbol{\omega}) = \begin{cases} 0 & \text{if } \omega_1 = 0 \quad (\text{i.e., } \boldsymbol{\Omega} = \boldsymbol{\omega}) \\ -2J_2\omega_1\omega_3 \mathbf{j}_M + 2J_3\omega_1\omega_2 \mathbf{k}_M & \text{if } \omega_1 \neq 0 \end{cases} \tag{46}$$

The gravitational force, passing the COM, does not induce the moment. In the *M*-coordinate system, the moment of gyration tensor for the axially symmetric cylinder is a diagonal matrix

$$\mathbf{J} = \begin{bmatrix} J_1 & 0 & 0 \\ 0 & J_2 & 0 \\ 0 & 0 & J_3 \end{bmatrix} \tag{47}$$

where $J_1$, $J_2$, and $J_3$ are the moments of inertia. The buoyancy force induces the moment in the $\mathbf{j}_M$ direction if the COM does not coincide with the COV (i.e., $\chi \neq 0$),

$$\mathbf{M}_b = |\mathbf{F}_b| \chi \cos \psi_2 \mathbf{j}_M \tag{48}$$

**6.2 IMPACT35-Cylindrical.** The three-dimensional model, usually called IMPACT35 (written in MATLAB), is the third generation of the Navy's mine impact burial prediction model. For cylindrical mines, it is called IMPACT35-Cylindrical or IMPACT35C. It was developed to solve the six scalar equations (43) and (44) to obtain $(x, y, z, \omega_1, \omega_2, \omega_3)$. From the angular velocity $(\omega_1, \omega_2, \omega_3)$, the three angles determining the mine orientation $(\psi_1, \psi_2, \psi_3)$ can be obtained,

$$\frac{d\psi_1}{dt} = \omega_1, \quad \frac{d\psi_2}{dt} = \omega_2, \quad \frac{d\psi_3}{dt} = \omega_3$$

The external forcing for IMPACT35 consists of drag force $\mathbf{F}_d$ and torque $\mathbf{M}_d$, as well as lift force $\mathbf{F}_l$ and torque $\mathbf{M}_l$. All these external forces and torques are calculated in the *F*-coordinate system. The model includes cylindrical and noncylindrical mines. In this subsection, the cylindrical mine is taken as an example for illustration.

*6.2.1 Drag and Lift Forces.* Two features of the drag and lift coefficients (Reynolds number dependent and asymmetry in along- and across-mine main axis) distinguish IMPACT35 from IMPACT25/28. The drag and lift forces are calculated using the *F*-coordinate system. Let $(C_{d1}, C_{d2})$ be the drag coefficients along- and across-mine main axis and $(f_1, f_2, f_3)$ be the added-mass corrections $(f_1, f_2, f_3)$ in the three directions of the *F*-coordinate system.

The total drag force along $\mathbf{i}_F$ (i.e., relative flow along the cylinder's main axis) is calculated by

$$F_{d1} = C_{td1}(t) V_1, \quad C_{td1}(t) \equiv C_{d1} \frac{\pi R^2}{2} \frac{\rho_w}{(1+f_1)} |V_1(t)| \tag{49}$$

$C_{d1}$ is almost independent of the axial Reynolds number (Re) when $\text{Re} > 10^4$ but dependent on the cylinder's aspect ratio [33],

$$C_{d1} = \begin{cases} 1.0 & \text{if } \delta > 8 \\ 0.75 + \delta/32.1934 + 0.09612/\delta^2 & \text{if } 8 \geqslant \delta > 0.5 \\ 1.15 & \text{if } \delta \leqslant 0.5 \end{cases}$$

The total drag force along $\mathbf{j}_F$ (i.e., relative flow across the cylinder) is calculated by

$$F_{d2} = R\int_{-L/2-\chi}^{L/2-\chi} C_{d2}(V_2')^2 \frac{\rho_w}{(1+f_2)}dx, \quad V_2'(x) = V_2 - \omega_3^F x \quad (50)$$

where $V_2'$ is the water-to-cylinder velocity at the surface in the $\mathbf{j}_F$ direction and an empirical formula is used for calculating $C_{d2}$ [39],

$$C_{d2} = \begin{cases} 1.9276 + 8/\text{Re} & \text{if Re} \leqslant 12 \\ 1.261 + 16/\text{Re} & \text{if } 12 < \text{Re} \leqslant 180 \\ 0.855 + 89/\text{Re} & \text{if } 180 < \text{Re} \leqslant 2000 \\ 0.84 + 0.00003\ \text{Re} & \text{if } 2000 < \text{Re} \leqslant 12{,}000 \\ 1.2 - 4/\delta & \text{if } 12{,}000 < \text{Re} \leqslant 150{,}000, \quad \delta \geqslant 10 \\ 0.835 - 0.35/\delta & \text{if } 12{,}000 < \text{Re} \leqslant 150{,}000, \quad 2 \leqslant \delta < 10 \\ 0.7 - 0.08/\delta & \text{if } 12{,}000 < \text{Re} \leqslant 150{,}000, \quad \delta < 2 \\ 1.875 - 0.0000045\ \text{Re} & \text{if } 150{,}000 < \text{Re} \leqslant 350{,}000 \\ 1/(641550/\text{Re} + 1.5) & \text{if Re} > 350{,}000 \end{cases} \quad (51)$$

The drag force along $\mathbf{k}_F$ is calculated by

$$\mathbf{F}_{d3} = \left[ C_{d2}R\frac{\rho_w}{(1+f_2)}\omega_2^F|\omega_2^F|\left(\int_0^{L/2-\chi} x^2dx - \int_{-L/2-\chi}^{0} x^2dx\right)\right]\mathbf{k}_F \quad (52)$$

The water-to-cylinder velocity determines the lift force [40],

$$\mathbf{F}_l = \left[\frac{C_{tl}(t)}{L}\int_{-L/2-\chi}^{L/2-\chi} V_2'(x)dx\right]\mathbf{k}_F, \quad C_{tl}(t) \equiv C_l LR\frac{\rho_w}{(1+f_2)}|V_2| \quad (53)$$

where $C_l$ is the lift coefficient. An empirical formula is used for calculating $C_l$ [41],

$$C_l = \begin{cases} 2\omega_1 R/V_2 & \text{if } \omega_1 R/V_2 \leqslant 4 \\ 8 + 0.24(\omega_1 R/V_2 - 4) & \text{if } \omega_1 R/V_2 > 4 \end{cases} \quad (54)$$

*6.2.2 Drag and Lift Torques*. For an axially symmetric cylinder, the moment of the hydrodynamic force in $\mathbf{i}_F$ direction is not caused by the drag and lift forces, but by the viscous fluid. The moment of the viscous force of steady flow between two rotating cylinders with the common axis is calculated by [42]

$$M = 4\pi\mu\frac{r_1^2 \cdot r_0^2}{r_1^2 - r_0^2}(\omega_1 - \omega_0)$$

where $(r_1, r_0)$ and $(\omega_1, \omega_0)$ are the radii and the angle velocities of the inner and outer cylinders; $\mu$ is the dynamic viscosity. The moment of the viscous force on one rotating cylinder is the limit case of the two rotating cylinders as $r_0 \to \infty$ and $\omega_0 = 0$. The moment of the viscous force around $\mathbf{i}_F$ is calculated by

$$\mathbf{M}_{v1} = -C_{m1}\omega_1\mathbf{i}_F, \quad C_{m1} \equiv \pi\mu L d^2 \quad (55)$$

Same as the hydrodynamic forces, the torques along the $\mathbf{j}_F$ and $\mathbf{k}_F$ axes, $(\mathbf{M}_{d1}, \mathbf{M}_{d2}, \mathbf{M}_l)$, are calculated. When the cylinder rotates around $\mathbf{j}_F$ with the angular velocity $\omega_2^F$, the drag force causes a torque on the cylinder in the $\mathbf{j}_F$ direction,

$$\mathbf{M}_{d2} = \left[-\omega_2^F|\omega_2^F|\int_{-L/2-\chi}^{L/2-\chi} C_{d2}R\frac{\rho_w}{(1+f_r)}x^2|x|dx\right]\mathbf{j}_F \quad (56a)$$

where $f_r$ is the added-mass factor for the moment of drag and lift forces. If the water-to-cylinder velocity or the cylinder mass distribution is nonuniform ($\chi \neq 0$), the drag force causes a torque on the cylinder in the $\mathbf{k}_F$ direction,

$$\mathbf{M}_{d3} = \left[\int_{-L/2-\chi}^{L/2-\chi} C_{d2}R\frac{\rho_w}{(1+f_r)}(V_2 - \omega_3^F x)^2 x dx\right]\mathbf{k}_F \quad (56b)$$

The lift force exerts a torque on the cylinder in the $\mathbf{j}_F$ direction,

$$\mathbf{M}_{l2} = \left[-\int_{-L/2-\chi}^{L/2-\chi} C_l R\frac{\rho_w}{f_{kr}}(V_2 - \omega_3^F x)x dx\right]\mathbf{j}_F \quad (57)$$

*6.2.3 Interfacial Treatment*. Computation of buoyancy and hydrodynamic forces $(\mathbf{F}_b, \mathbf{F}_h)$ and torques $(\mathbf{M}_b, \mathbf{M}_h)$ is more complicated for a cylinder penetrating through air-water and water-sediment interfaces than falling through a single medium such as water. At the instance when the cylinder penetrates into an interface, three situations may exist: the cross section is a complete ellipse (Fig. 9(*a*)), a cutoff ellipse with one side straight line (Fig. 9(*b*)), or a cutoff ellipse with two straight lines (Fig. 9(*c*)). The interface separates the cylinder to two parts. Each part contains a noncylinder $D$ and a subcylinder $C$ (Fig. 10). Let $(L_c, L_d)$, $(\Omega_c, \Omega_d)$, and $(\Pi_c, \Pi_d)$ be the lengths, surfaces, and volumes of $[C, D]$, and $(h_1, h_2)$ be the depths of the two sides of $D$ (Fig. 11). The characteristics of the geometric parameters $(L_c, h_1, h_2)$ are listed in Table 1. The COV for the portion $[C, D]$ is called the partial COV (PCOV). With this treatment, the drag and lift forces and torques at the two parts $C$ and $D$ can be computed separately [36].

*6.2.4 Sediment Resistance*. In the two-dimensional models, IMPACT25/28, the pertinent parameters are sediment density and bearing strength. The bearing strength is calculated simply by ten times the shear strength, which is not very realistic. In fact, when the mine impacts and penetrates into the sediment, it will create a large transient pore pressure in the sediment that causes ruptures in the sediment and influences the resistance force on the mine

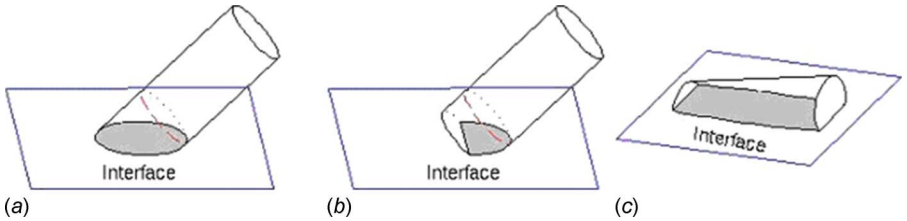


**Fig. 9 Three patterns of cylinder penetration with the cross section being (*a*) a complete ellipse (*b*) cutoff ellipse with one side straight line, and (*c*) a cutoff ellipse with two side straight lines (after Chu and Fan [36])**

surface [11,36], which is not simply ten times the shear strength. In the three-dimensional model (IMPACT35), two distinct methods (delta and bearing factor) are used to compute total sediment resistance force and torque.

*(a) Delta method*. The delta method is developed on the assumption that the mine pushes the sediment and leaves space in the wake as it impacts and penetrates into the sediment. This space is refilled by water and the water cavity is produced (Fig. 12). At the instance of the penetration, the total sediment shear resistant force on the mine surface is calculated by [36]

$$\mathbf{F}^s = \int_{\sigma_{sed}} \Delta\boldsymbol{\tau}[\mu G(V)S(z)]d\sigma - \int_{\sigma_{sed}} \mathbf{n}\left[\left(\Delta\int_z^{z_{ws}} \rho_s(z')g dz'\right) + \rho_w g(z_{ws}-z)\right]d\sigma + \mathbf{k}\frac{\pi}{8}\rho_s(z)\left(\frac{gw}{k_p}+\frac{1+e_v}{e_v}\frac{dw}{dt}\right)B^3 \quad (58)$$

where in the right-hand side the first term is the shear resistance force, the second term is the buoyancy force, and the third term is the pore water pressure. $S(z)$ is the sediment shear strength, $G(V)$ is the impact function, $V$ is the mine translation speed, $\rho_s(z)$ is the sediment wet density (usually obtained from the sediment data), $(\mathbf{n},\boldsymbol{\tau})$ are unit vectors normal (outward positive) and tangential to the mine surface, $z_{ws}$ represents the vertical coordinate of the water-sediment interface $k_p$ is the permeability coefficient ($10^{-4}$ m s$^{-1}$, [43]), $e_v$ ($\sim$0.50) is the void ratio, and $B$ is the length of the rupture line. The step function $\Delta$ is defined by

$$\Delta = \begin{cases} 1, & \mathbf{v}\cdot\mathbf{n} \geqslant 0 \\ 0, & \mathbf{v}\cdot\mathbf{n} \leqslant 0 \end{cases} \quad (59)$$

which shows that the sediment buoyancy and shear resistance forces act when the cylinder moves toward it. Let $\mathbf{v}_n$ be the normal velocity. The tangential velocity is represented by

$$\mathbf{v}_\tau = \mathbf{v} - \mathbf{v}_n \quad (60)$$

The tangential unit vector $(\boldsymbol{\tau})$ is defined by

$$\boldsymbol{\tau} = -\frac{\mathbf{v}_\tau}{|\mathbf{v}_\tau|} \quad (61)$$

which is opposite to $\mathbf{v}_\tau$ (Fig. 13).

The sediment resistance torque $(\mathbf{M}^s)$ is calculated by

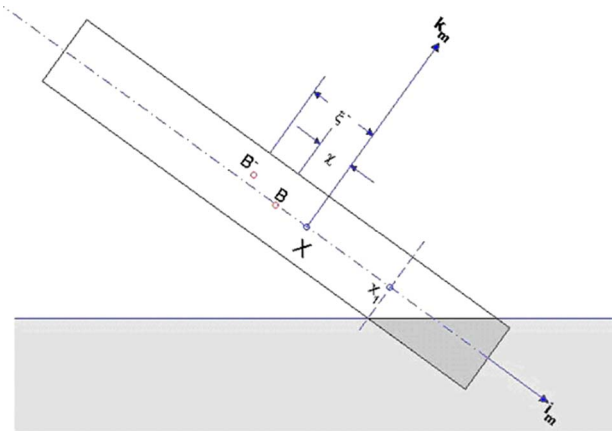


**Fig. 10 Illustration of PCOV ($B^-$), $x_1$, and $\xi^-$ for the tail part [$C^{(1)}, D^{(1)}$] for the case in Fig. 9(*a*) (after Chu and Fan [36])**

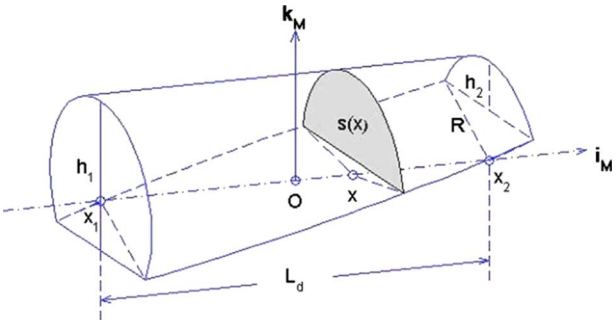


**Fig. 11 Geometry of part $D^{(1)}$ (after Chu and Fan [36])**

**Table 1 Geometric parameters during the cylinder penetration [36]**

| | $L_c$ | $h_1$ | $h_2$ |
|---|---|---|---|
| Upper and lower parts of Fig. 9(*a*) | >0 | 2*R* | 0 |
| Upper part of Fig. 9(*b*) | >0 | 2*R* | 0–2*R* |
| Lower part of Fig. 9(*b*) | 0 | 0–2*R* | 0 |
| Upper and lower parts of Fig. 9(*c*) | 0 | 0–2*R* | 0–2*R* |

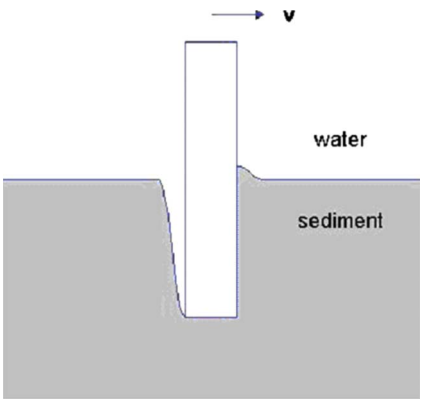


**Fig. 12 The impact (resistant) force exerted on the part of the mine surface moving toward the sediment (after Chu and Fan [36])**

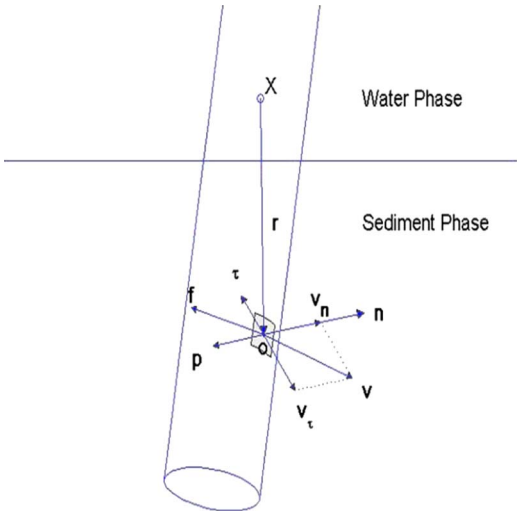


**Fig. 13 Momentum and angular momentum balance for mine penetration through the water-sediment interface**

$$\mathbf{M}^s = \int_{\sigma_{sed}} (\mathbf{r} \times \boldsymbol{\tau})[\Delta\mu G(V)S(z)]d\sigma + \int_{\sigma_{sed}} (\mathbf{r} \times \mathbf{n})\left[\left(\Delta\int_z^{z_{ws}} \rho_s(z')gdz'\right) + \rho_w g(z_{ws} - z)\right]d\sigma + (\mathbf{r}_{pw} \times \mathbf{k})\frac{\pi}{8}\rho_s(z)\left(\frac{gw}{k} + \frac{1+e_v}{e_v}\frac{dw}{dt}\right)B^3 \quad (62)$$

where $\mathbf{r}_{pw}$ is the position vector (in the $M$-coordinate) indicating the location of the cylinder's rupture line.

*(b) Bearing factor method*. The bearing factor method is based on the fact that the shear resistance force ($\mathbf{F}_r^s$) is in the opposite direction of $\mathbf{v}$ and acts on the mine. Its magnitude is proportional to the product of the sediment shear strength ($S$) and the rupture area ($A$ is projection of sediment-contacting area perpendicular to the velocity $\mathbf{V}$) with a non-negative bearing factor $N$ [44],

$$\mathbf{F}_r^s = -\int_{\sigma_{sed}} \boldsymbol{\tau} N(p,v)SAd\sigma, \quad N \geq 0 \quad (63)$$

The sediment resistance torque includes the hydrodynamic and shearing resistance torques,

$$\mathbf{M}^s = \int_{\sigma_{sed}} \{\mathbf{r} \times \mathbf{f}_h^s - [N(p,v)SA]\mathbf{r} \times \boldsymbol{\tau}\}d\sigma \quad (64)$$

Here, $p$ is the non-dimensional penetration depth scaled by the diameter ($2R$). The sediment density and shear strength $S$ in Eqs. (63) and (64) are measured. The bearing factor increases with $p$ and decreases with the decreasing speed,

$$N(p,v) = [\mu_1 p^{\mu_2}]\left[1 + \lambda \log\left(\frac{v}{v_{\text{cri}}}\right)\right] \quad (65)$$

where $\lambda$ is the $v$-effect parameter, $(\mu_1, \mu_2)$ are the $p$-effect parameters [16], and $v_{\text{cri}}$ is the critical speed.

*6.2.5 Pseudocylinder parametrization*. The Navy operational mines are usually not cylindrical. It is important to develop a model with more general shapes such as with nose and tail. Pseudocylinder parametrization was proposed for noncylindrical mines [35]. For a near-cylindrical mine with nose and tail falling through a single medium or multiple media, the buoyancy force and torque are relatively easy to calculate. But the hydrodynamic forces (lift, drag) and torques are difficult to compute. A feasible way is to transform a mine with nose and tail to a cylindrical mine (i.e., called the pseudocylinder parameterization). An axially symmetric mine usually consists of three parts: cylindrical body with radius of $R$, nose, and tail (Fig. 14). The lengths of the mine, nose, and tail are $L$, $L_n$, and $L_t$. A pseudocylinder is defined with the following features: same radius ($R$) of the mine's cylindrical body and the same volume as the original mine (Fig. 15). It consists of three parts: original cylindrical body, and equivalent cylinders for nose and tail. Let $(\Pi, \Pi_n, \Pi_t)$ be the volumes of the mine, nose, and tail. The equivalent cylinder has length

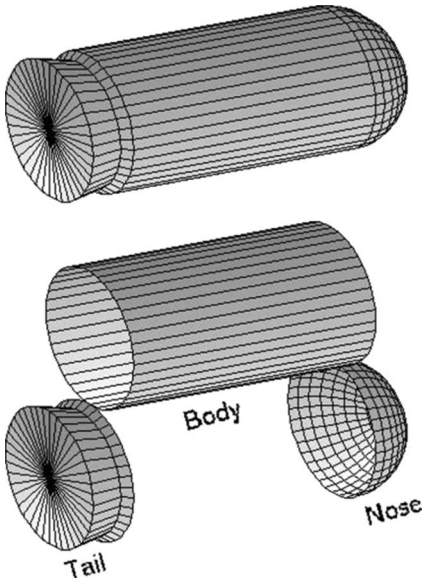


**Fig. 14 Mine with nose, tail, and cylindrical body (after Chu and Fan [35])**

$$L_{ne} = \frac{\Pi_n}{\pi R^2}$$

for the nose, and

$$L_{te} = \frac{\Pi_t}{\pi R^2}$$

for the tail. Let $(c_c, c_m)$ be the mine's midpoint on the main axis and the COM position, and let $c_{ev}$ be the COV of the pseudocylindrical mine (Fig. 15). The gravity is downward and passing

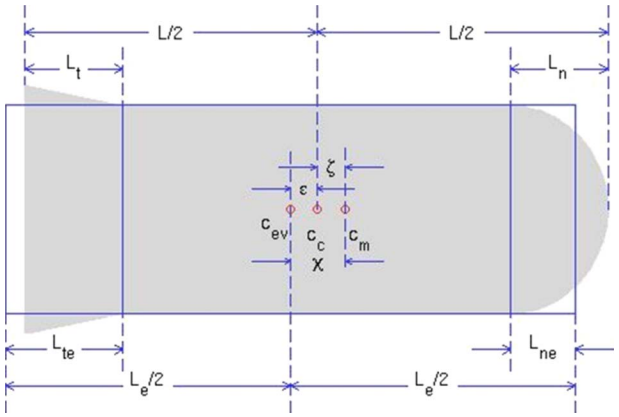


**Fig. 15 Location of $c_v$, $c_{ev}$, and $c_m$. Here, $\varepsilon$ is the distance between $c_v$ and $c_m$; $\chi$ is the distance between $c_{ev}$ and $c_m$ (after Chu and Fan [35]).**

Table 2 Physical parameters of the model mines in the NSWC-Carderock experiment [47]

| Mine | Mass (kg) | $\rho$ ($10^3$ kg m$^{-3}$) | $L$ (m) | $J_1$ (kg m$^2$) | $J_2$ ($J_3$) (kg m$^2$) | $\chi$ (m) |
|---|---|---|---|---|---|---|
| 1 | 16.96 | 1.60 | 0.505 | 0.0647 | 0.356 | 0 |
| 2 | 22.27 | 2.10 | 0.505 | 0.0806 | 0.477 | 0 |
| 3 | 34.93 | 1.60 | 1.010 | 0.1362 | 2.900 | 0 |
| 4 | 45.85 | 2.10 | 1.010 | 0.1696 | 3.820 | 0 |
| 5 | 45.85 | 2.10 | 1.010 | 0.1693 | 3.940 | 0.0045 |
| 6 | 45.85 | 2.10 | 1.010 | 0.1692 | 4.570 | −0.077 |

through $c_m$. The buoyancy force is upward and passing through $c_{ev}$. Let $\varepsilon_1$ be the distances between $c_c$ and $c_m$,

$$\varepsilon_1 = \frac{L_n - L_{ne}}{2} - \frac{L_t - L_{te}}{2} \tag{66}$$

Let $\varepsilon_2$ be the displacement from $c_c$ to $c_m$ that is easy to determine if COM is given. Let $\chi$ be the displacement from $c_{ev}$ to $c_m$, that is, calculate

$$\chi = \varepsilon_1 + \varepsilon_2 \tag{67}$$

Both $\chi$ and $\varepsilon_2$ can be positive and negative. The positive values refer to nose-down case, i.e., the point $c_m$ is lower than the point $c_{ev}$ for positive $\chi$ and the point $c_c$ is lower than the point $c_{ev}$ for positive $\varepsilon_2$.

**6.3 Mine Impact Burial Experiment for Model Verification.** The value added of three-dimensional model (IMPACT35) versus two-dimensional model (IMPACT25/28) is verified by several recent mine impact burial experiments (Table 2): Mine Impact Burial Experiment (MIBEX) at Monterey Bay on May 22, 2000 [9,31,32], Mine Drop Experiment (MIDEX) at NPS swimming pool in June 2001 [45,6,10,13,16,34], MIDEX at NSWC-Carderock Explosion Test Pond on September 10-14, 2001, and MIDEX at NSWC-Corpus Christi [46–48]. The MIDEX at the Baltic Sea experiment was conducted in June 2003 by the German Federal Armed Forces Underwater Acoustic and Marine Geophysics Research Institute [49,50] with the full-size optical mine, which is allowed to free fall from the wench. During these experiments, various model mines (most cylindrical) were released into the water. The mine trajectories were recorded by underwater high-speed video cameras. The mine burial depths were also observed by the diver (in MIBEX-Monterey Bay) and optical instruments (in MIDEX-Baltic Sea).

The two-dimensional model (IMPACT25/28) and three-dimensional model (IMPACT35) are integrated using the same mine parameters (such as the density ratio, length, radius, and distance between COV and COM) and mine drop initial conditions (speed and orientation) as in the mine drop experiments. The value added of IMPACT35 versus IMPACT25/28 is verified through comparison between the modeled and observed mine trajectories and burial depths.

**6.4 Trajectory in Water Column.** Detailed verification of trajectory prediction in the water column by IMPACT35 and IMPACT25/28 has been reported in Ref. [11] using data from MIDEX at NPS and MIDEX at NSWC-Caderock. For near horizontal release, the 3D model (IMPACT35) simulated trajectory agrees well with the observed trajectory with the same travel time (1.91 s) of mine passing through the water column. For near 45 deg release, the 3D model (IMPACT35) simulated trajectory and travel time agree well with the observed trajectory. However, the 2D model (IMPACT28) has much less capability to predict the cylinder trajectory in the water column with near horizontal and 45 deg release. For near vertical release, the 3D model (IMPACT35) simulated trajectory agrees well with the observed trajectory with the same straight pattern and the same travel time (1.83 s) of mine passing through the water column. However, the existing 2D model (IMPACT28) does not predict the travel time well.

**6.5 Burial Depth.** MIBEX-Monterey Bay was conducted on the R/V John Martin on May 23, 2000 [9,31]. The barrel with a density ratio of 1.8 was treated as model mine and released horizontally while touching the surface. The initial conditions are

$$x^{(0)} = y^{(0)} = z^{(0)} = 0, \quad u^{(0)} = v^{(0)} = w^{(0)} = 0$$

$$\psi_2^{(0)} = 90 \text{ deg}, \quad \psi_1^{(0)} = \psi_3^{(0)} = 0, \quad \omega_1^{(0)} = \omega_2^{(0)} = \omega_3^{(0)} = 0 \tag{68}$$

This would be to eliminate any chance of inertial effects caused by uneven introduction into the air-sea interface. This also set the initial velocity to zero. The barrel was released 17 times. The diver would snap the quick-release shackle on the barrel and then dive down to conduct measurements. The average depth of the water was 13 m. Since it was uncertain the path the barrel would follow, both the releasing diver and a second safety diver would stay on the surface until after the barrel had dropped. Once reaching the bottom, one diver would take penetration measurements using a meter stick marked at millimeter increments while the other would take a gravity core. After 17 drops, the divers began to run out of air and results were not varying greatly so the decision was made to end the experiment. The gravity cores were taken immediately to the USGS Laboratories in Menlo Park, CA to get the sediment density and shear strength profiles (Fig. 16).

For sediment resistance force, the two-dimensional model (IMPACT25/28) uses ten times shear strength as the bearing strength. The three-dimensional model (IMPACT35) uses the delta or bearing factor method (see Sec. 6.2.4). After running the two models (IMPACT35 and IMPACT25/28) for each gravity core regime $[\rho_s(z), S(z)]$ from the initial conditions (69), the burial depths were compared with measured burial depth data (Fig. 17).

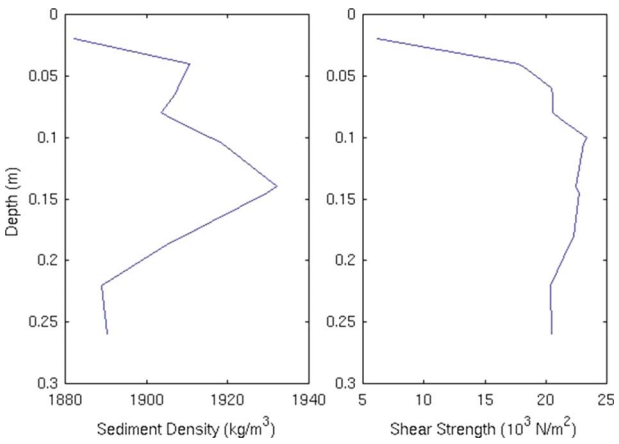


**Fig. 16 Mean sediment density $\rho_s(z)$ and shear strength $S(z)$ profiles in the Monterey Bay collected during the cylinder drop experiment on May 31, 2000**

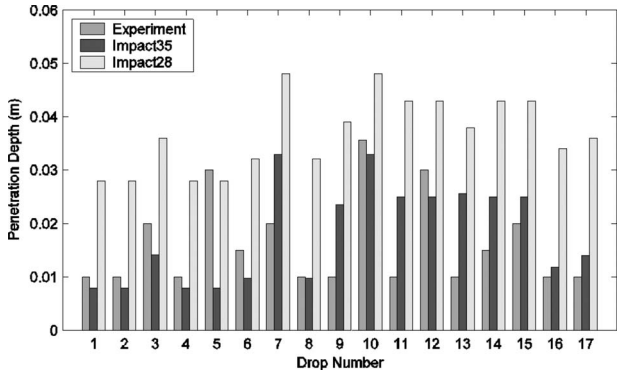


**Fig. 17 Observed (MIBEX-NPS) and predicted (IMPASCT25/28 and IMPASCT35 with Delta method) burial depths: (*a*) direct comparison and (*b*) scatter diagram. Note that the two-dimensional model (IMPACT25/28) predicts the burial depth five to ten times larger than the observed depth, and IMPACT35 with Delta method performs much better than IMPACT/28 (after Chu and Fan [36]).**

As evident, IMPACT35 improves the prediction capability. The 2D model (IMPACT25/28) overpredicts the actual burial depth by an order of magnitude on average. However, the 3D model (IMPACT35) predicts the burial depth reasonably well without evident overprediction. Since the gravity cores were taken for approximately 2–3 m from the impact location, several cores were taken for each drop. This allowed an average to be calculated in order to yield more accurate data for each drop. Recently, Chu and Fan [11] compared the delta and bearing factor methods in IMPACT35C for sediment resistance using the Baltic Sea experiment data and found that the bearing factor method is better than the delta method.

## 7 Modeling of Operational Mines

**7.1 Shape Effect.** Main limitation of IMPACT35C is its utilization for cylindrical and near-cylindrical mines only. Shape is a significant issue if the model is used operationally because the most popular mines such as Rockan and Manta are far from cylindrical (Fig. 18). To model the maneuvering of noncylindrical mines in water column, the most important issue is to determine the hydrodynamic (drag and lift) force and torque since there is no existing formula for calculating the drag and lift forces and torques for noncylindrical objects. Shape effect is more tenuous due to the lack of test data.

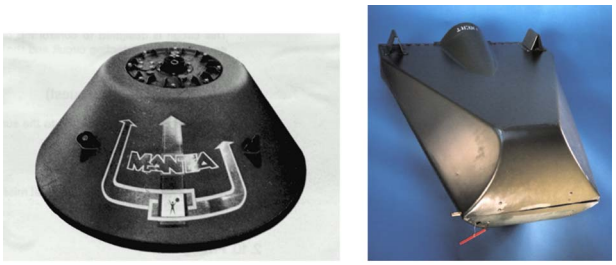


(*a*) (*b*)

**Fig. 18 Operational mines: (*a*) Manta, and (*b*) Rockan. Here, the Manta is an anti-invasion bottom mine, produced primarily by the Italian firm Whitehead Alenia. It is shaped as a frustum with a GRP casing, triggered either acoustically or magnetically. The Manta has a shelf life of 30 years and will operate for 17 months after activation. The Rockan (made in Sweden) has a gliding shape, which allows mine laying over a wide area while covering the minimal distance; its low-profile stealth shape makes it difficult to detect. Its casing is also constructed of GRP.**

**Table 3 Physical parameters of Rockan mines**

| | |
|---|---|
| Diameter | 0.980 m |
| Height | 0.440 m |
| Weight | 220 kg |
| Charge | 130 kg (HBX-3) |
| Operating depth | 3–100 m |

**Table 4 Physical parameters of Manta mines**

| | |
|---|---|
| Length | 1.015 m |
| Width | 0.800 m |
| Height | 0.385 m |
| Weight | 190 kg |
| Charge | 105 kg (Cemtex) |
| Operating depth | 105 kg |

MIDEX-II at NPS, conducted in September 2005, is a continuation of mine drop experiments with operational mine shapes [51,52]. In that experiment, the overall shape of the mine was noncylindrical mines. In addition to a sphere and semihemispherical Gumdrop shape, two shapes were specifically chosen to represent real world bottom mines: the Manta and Rockan.

The Manta (Fig. 18(*a*)) is an anti-invasion bottom mine, produced primarily by the Italian firm Whitehead Alenia. It is shaped as a combined frustum and flat cylinder with a glass reinforced plastic (GRP) casing, triggered either acoustically or magnetically. The Manta has a shelf life of 30 years and will operate for 17 months after activation.

The BGM-100 Rockan (Fig. 18(*b*)) is an acoustic and magnetic mine, produced by Sweden. It has a gliding shape, which allows mine laying over a wide area while covering the minimal distance. The low-profile stealth shape makes it difficult to detect. Its casing is also constructed of GRP. Both the Manta and Rockan are made even stealthier by having anechoic coatings and being made of

**Table 5 Physical and geometrical features of model mines used in MIDEX-II**

| Model | Mass | Density | Dimensions | |
|---|---|---|---|---|
| Manta bottom influence mine shape | 1145.0 g | 1.615 g/cm$^3$ | *D* (Bottom)<br>*D* (Top)<br>*H*<br>Scale<br>Distance from COM to COV | 15.0 cm<br>7.0 cm<br>6.2 cm<br>1/6<br>+0.373 cm *Z*-axis |
| Rockan bottom influence mine shape | 813.0 g | 1.388 g/cm$^3$ | *L*<br>*W* (Back)<br>*W* (Front)<br>*H* (Back)<br>*H* (Front)<br>Scale<br>Distance from COM to COV | 16.0 cm<br>7.8 cm<br>13.3 cm<br>6.3 cm<br>3.8 cm<br>1/6<br>0 cm |
| Generic spherical shape | 1692.0 g | 1.335 g/cm$^3$ | *D*<br>Distance from COM to COV | 13.0 cm<br>0 cm |
| Gumdrop hemispherical shape | 2815.0 g | 1.722 g/cm$^3$ | *D*<br>*H*<br>Distance from COM to COV | 14.9 cm<br>13.3 cm<br>0 cm |

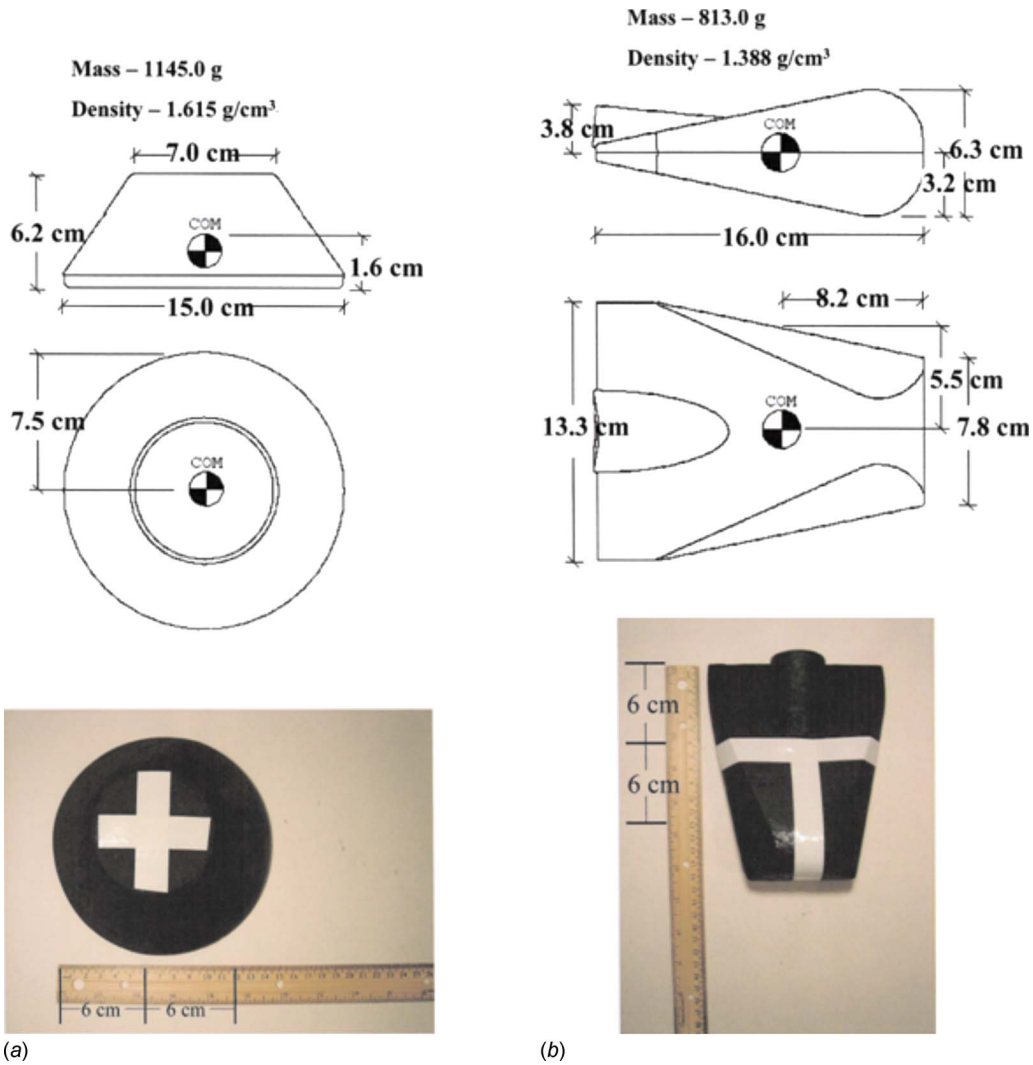


**Fig. 19 Side and top views of the model mines with different shapes for MIDEX-II experiment; (*a*) Manta and (*b*) Rockan. The construction of these model mines consisted of a three-part product process: prototype development, mold construction, and test shape casting, and finishing. This process was necessary to facilitate more efficient experimentation and to reduce the production cost of the experimental test shapes.**

nonferrous materials to reduce the mines' acoustic and magnetic signatures. Tables 3 and 4 show the geometric and physical characteristics of Rockan and Manta mines.

**7.2 MIDEX-II.** The major objective of the MIDEX-II was the collection of trajectory data for operational mine shapes. Each shape was dropped just above the surface of the water and filmed with a pair of high-speed cameras as the model mines fall through the water column. Each trajectory was then converted to an array of Cartesian coordinates (*E*-coordinate) and analyzed with software specifically designed to work with the high-speed cameras.

Mine shapes are selected based upon current and future operational relevance. A collection of four minelike polyester resin test shapes were used. These shapes include sphere, semihemispherical "Gumdrop" shape, a scale model of the Manta bottom mine, and a scale model of the Rockan bottom mine. The spherical mine is selected to serve as a "calibration" shape because its symmetry and equal weight distribution are about its three axes. The Gumdrop is similar in shape to but higher in density than the Sphere. The Gumdrop is selected to act as a kind of "traditional" shape of bottom sea mines, though no mine was specifically represented. Table 5 shows the physical and geometrical characteristics of the four model mines. Figure 19 shows the geometric features, horizontal, and lateral views of Matha and Rockan model mines.

MIDEX-II was conducted at the Monterey Bay Aquarium Research Institute (MBARI) Unmanned Underwater Vehicle Test Tank (Fig. 20(*a*)). Enclosed inside a large building, this $10\times15\times10$ m$^3$ tank is filled with "standard sea water." This water is maintained by an ozone filtration system, with no impurities that save the remnants of dye placed into the tank several weeks prior to the experiment. The faint coloration has no effect on the shape trajectories, but it did add some difficulty illuminating the tank. Hence the video data quality is somewhat degraded. A sliding bridge, on which the slanted board is mounted, spanned the width of the tank. Figure 20(*b*) describes the measurements of the tank and placement of the drop zone, cameras, and lighting.

The tank is used to simulate the littoral operating environment with the scaled depth ranging to 54.9 m (180 ft); however, the nature of the viewing windows only allows data collection to a scaled depth of roughly 18.29 m (60 ft). The tank has no current and no wind blowing over its surface. To aid in shape recovery, a $9\times13$ m$^2$, 2 cm netting was mounted to a constructed 1.9 cm diameter PVC piping horizontal grid and placed at the bottom of the tank out of camera view. At the end of a run, the net that contained the shapes was retrieved using a series of pulleys placed

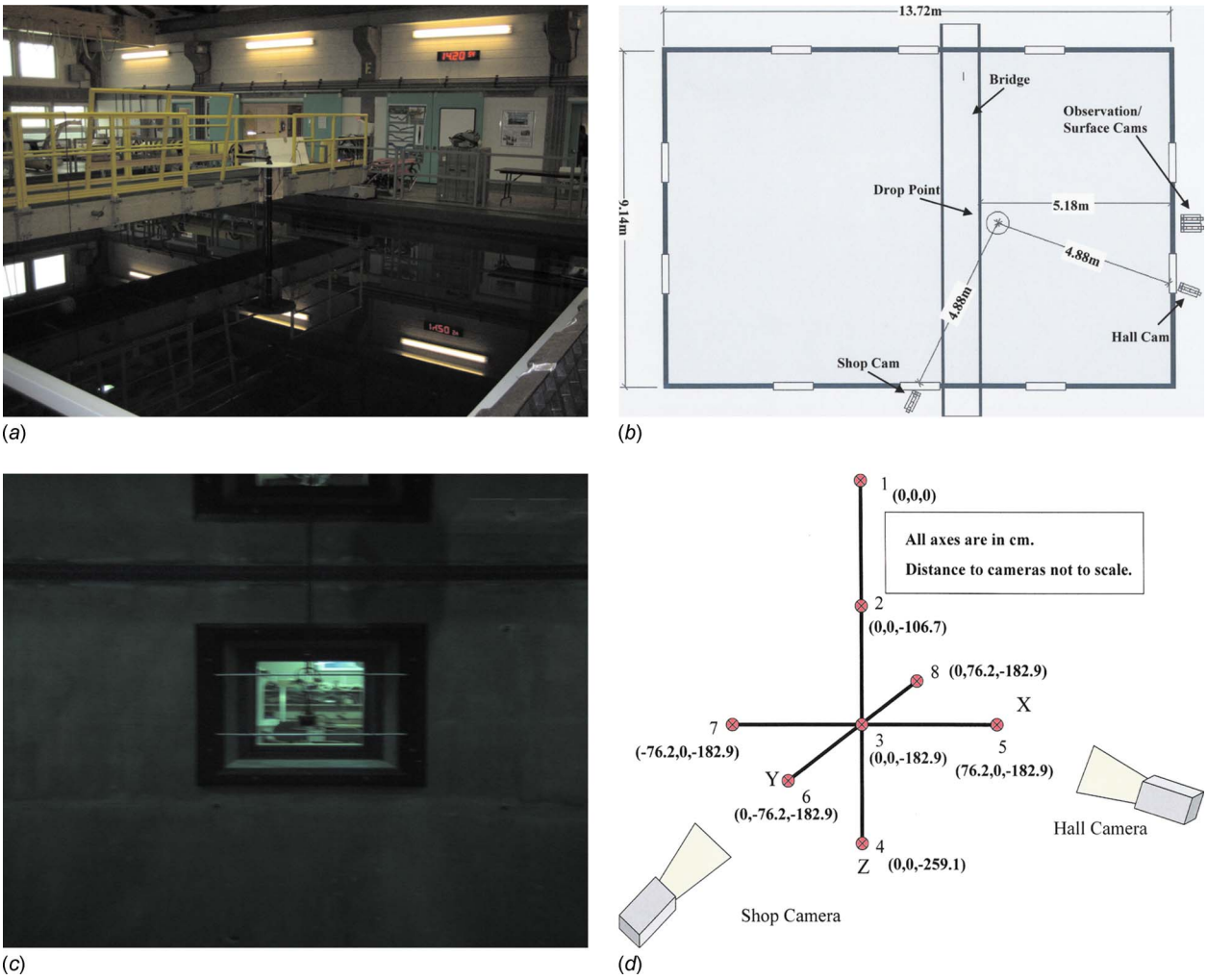


**Fig. 20 MIDEX-II setup: (*a*) MBARI test tank facility (structure above water is a movable bridge), (*b*) top view of the two video cameras, (*c*) view from underwater viewing window, and (*d*) calibration test cross. Here, the MBARI test tank (10 $\times$15$\times$10 m$^3$) was filled with "standard sea water." This water was maintained by an ozone filtration system, with no impurities that save the remnants of dye placed into the tank several weeks prior to the experiment. A sliding bridge, on which the slanted board was mounted, spanned the width of the tank (see (*a*)). Eight viewing windows (*c*) were 1.83 m (6 ft) below the surface of the water. The two viewing windows used were selected because of the unobstructed and near perpendicular view to the mine drop spot.**

at the four corners of the tank. Two large dark 4.57$\times$5.18 m$^2$ tarpaulins were placed along the tank walls behind the camera views to assist the cameras and software with distinguishing the falling mine shapes from the tank background. Eight viewing windows (Fig. 20(*c*)) are 1.83 m (6 ft) below the surface of the water. The two viewing windows are selected because of the unobstructed and near perpendicular view to the drop spot.

All the data were collected digitally using a network of high-speed and standard video equipment and computers. Data above the surface are collected using a pair of standard commercially available digital video camera, mounted on tripods, and located at the end of the pool directly in front of the testing zone. Both top cameras operated at a 30 Hz frame rate. The data camera uses a narrow view lens zoomed to focus on the area directly between the slanted board and the water surface, and is toggled on and off between test runs. The second camera used a wide-angle lens and was employed to record a video log of the experiment. This device ran continuously throughout the experiment.

Subsurface video data, used to determine the trajectory of the falling shapes, are collected using a pair of high-speed Photron FASTCAM PCI digital cameras (Fig. 20(*d*)). These cameras are mounted on tripods in two separate windows, at an angle of 70 deg in relation to one another so as to provide two, near orthogonal, views of the drop zone. After mounting and calibration, each camera station is covered with black plastic to block out any light source beside that which comes from the field of view. The cameras are synchronized, calibrated, and connected by a centrally located laptop computer via high-speed data cables. During testing, the cameras are operated using the Photron FASTCAM Viewer software at 512$\times$480 pixel resolution at full frame and recording rates of 125 Hz. To facilitate a wider field of view, both cameras are fitted with wide-angle lens. All data are recorded digitally on a standalone 200 Gbytes hard drive during the test phase. Additionally, to enhance the quality of the data during testing, the installed tank lighting system is turned to its maximum setting and a pair of 1000 W high intensity photography lights are mounted and used above the surface.

The mine drop experiment consists of releasing each shape vertically from about 0.3 m (1 ft) above the surface of the water. The entry of each shape into the water is recorded by the two above-surface video cameras. All subsurface data collection is facilitated by the two FASTCAM PCI high-speed cameras. The subsurface digital data are analyzed by 3D motion analysis software to deter-


(*a*)

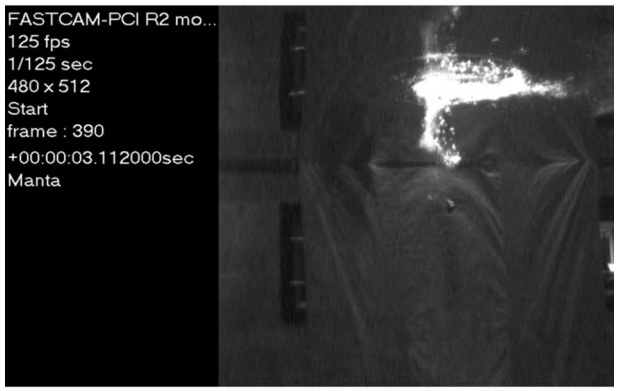


(*b*)

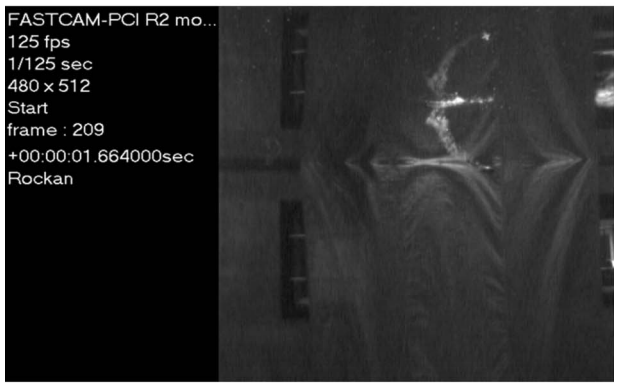


(*c*)

**Fig. 21 Examples of high-speed film frames for model mines. Here, the commercially available 3D motion analysis software, MAXTRAQ, was the primary tool utilized to perform this function.**

mine the trajectories of each shape. Overall, we have 15 drops of the Manta mine, 14 drops of the Rockan mine, 9 drops of the Gumdrop, and 13 drops of the Sphere. Initial velocities of all shapes as they entered the water are calculated later using the MAXTRAQ motion analysis software.

**7.3 Data Retrieval and Analysis.** Data retrieval has been accomplished following all the experimental test runs by converting the digital video imagery (Fig. 21) from each drop into an array of $(x,y,z)$ coordinate data. Commercially available 3D motion analysis software, MAXTRAQ, was the primary tool utilized to perform this function. Initially, the software is calibrated into the 3D coordinate reference system utilizing the pairs of calibration images obtained in the initial phase of the experiment. Following the calibration, both camera views were time synced and analyzed to determine the actual position of the shape in the $(x,y,z)$ coordinate field. Frame by frame analysis was performed with the software for each view by manually identifying and inputting one or two marker points associated with the model mine's position and orientation. For the Sphere and Gumdrop shapes, one marker point is used to identify the lowest position of the shape. For the Manta mine, Point 1 $(x_1,y_1,z_1)$ and Point 2 $(x_2,y_2,z_2)$ are chosen as the centers of the bottom diameter and top diameter. Examples of temporally varying data of $[x_1(t),y_1(t),z_1(t),x_2(t),y_2(t),z_2(t)]$ for the model Manta mine are listed in Table 6. From these data, the COM location $(x,y,z)$ and the orientation $(\psi_2,\psi_3)$ are calculated (Table 7).

For the Rockan mine, Point 1 $(x_1,y_1,z_1)$ is selected as the center of the narrow edge at the "electronics cylinder," and Point 2 $(x_2,y_2,z_2)$ is chosen as the center of the thicker edge of the shape opposite to Point 1. In frames where a marker point was obscured, the position of the marker (Point 1 or Point 2) is estimated visually based on the previous and next viewable frame. Following the analysis of both views, the automated functions of the software are employed to compile the 2D images into a calibrated array of 3D positional data. Examples of temporally varying data of $[x_1(t),y_1(t),z_1(t),x_2(t),y_2(t),z_2(t)]$ for the model Rockan mine are listed in Table 8. From these data, the COM location $(x,y,z)$ and the orientation $(\psi_2,\psi_3)$ are calculated (Table 9).

**7.4 Trajectory Patterns.** By analyzing the 2D and 3D plots of each shape drop, the general trajectory patterns of the four mines were obtained. The Sphere and Gumdrop mines are hydrodynamically simple, resulting in the quickest drop times in the experiment. The Gumdrop mine has the fastest mean travel time to 2.5 m depth (1.462 s). The Sphere favors a straight-arc trajectory (0.62 probability) over a curve-arc trajectory (0.38 probability). The Gumdrop favors a curve arc (0.56 probability) over both the straight arc (0.22 probability) and simple slant (0.22 probability).

The Manta and Rockan mines have more complicated shapes. Three trajectory patterns (flat spiral, side twist, and erratic) are

**Table 6 Examples of data for model Manta mines for a given initial velocity (3.116 m/s)**

| Time (s) | $x_1$ (m) | $y_1$ (m) | $z_1$ (m) | $x_2$ (m) | $y_2$ (m) | $z_2$ (m) |
|---|---|---|---|---|---|---|
| 0 | 0.2273 | 0.6953 | −0.6371 | −0.2273 | −0.6953 | 0.6371 |
| 0.016 | −0.3519 | 2.4886 | −2.821 | −1.1442 | −0.2139 | −3.5526 |
| 0.032 | −0.3707 | 0.7862 | −10.4696 | −0.7141 | −0.9996 | −9.4754 |
| 0.048 | −0.8714 | 0.531 | −16.3917 | −1.141 | −0.2135 | −13.5576 |
| 0.064 | −0.5257 | 0.1086 | −21.6666 | −0.8558 | −0.521 | −18.8631 |
| 0.08 | −0.2535 | −0.3598 | −26.5455 | −0.9635 | 0.2915 | −24.2111 |
| 0.096 | 0.0811 | −0.0842 | −30.5543 | −0.399 | −0.5669 | −28.8169 |
| 0.112 | 0.0192 | −0.8599 | −35.7727 | −0.8964 | −1.0305 | −33.9886 |
| 0.128 | −0.3806 | −2.0507 | −39.9809 | −1.0781 | −1.6472 | −38.5195 |
| 0.144 | −0.111 | −3.085 | −43.4884 | −0.236 | −2.4716 | −41.9996 |
| … | … | … | … | … | … | … |

**Table 7 Center of mass location ($x, y, z$) and orientation ($\psi_2, \psi_3$) for model Manta mine derived from the data shown in Table 6**

| Time (s) | $x$ (m) | $y$ (m) | $z$ (m) | $\pi/2-\psi_2$ | $\psi_3$ |
|---|---|---|---|---|---|
| 0 | 0 | 0 | 0 | −0.7165 | −1.8868 |
| 0.016 | −0.748 | 1.1373 | −3.1868 | 0.2542 | −1.856 |
| 0.032 | −0.5424 | −0.1067 | −9.9725 | −0.5003 | −1.7608 |
| 0.048 | −1.0062 | 0.1588 | −14.9747 | −1.2983 | −1.9182 |
| 0.064 | −0.6907 | −0.2062 | −20.2648 | −1.3224 | −2.0538 |
| 0.08 | −0.6085 | −0.0342 | −25.3783 | −1.1793 | 2.3993 |
| 0.096 | −0.1589 | −0.3256 | −29.6856 | −1.1973 | −2.3535 |
| 0.112 | −0.4386 | −0.9452 | −34.8807 | −1.0897 | −2.9573 |
| 0.128 | −0.7294 | −1.849 | −39.2502 | −1.0669 | 2.6172 |
| 0.144 | −0.1735 | −2.7783 | −42.744 | −1.1728 | 1.7718 |
| … | … | … | … | … | … |

identified for the Manta mine (Fig. 22(*a*)). Their characteristics are listed in Table 10. For example, the flat spiral pattern shows the Manta mine falling with its bottom side basically parallel to the *X-Y* plane and following a spiraling path. Table 11 shows the dependence of trajectory pattern and travel time (to 2.5 m depth) on initial speed and orientation of the Manta mine. Three trajectory patterns (flip-dive-flat, flat-spin, and swoop-flat-spin) are identified for the Rockan mine (Fig. 22(*b*)). Their characteristics are listed in Table 12. For example, the flip-dive-flat pattern shows the Rockan mine flipping once, going into a vertical dive, and settling into a slowly spinning horizontal orientation for the remainder of the drop. Table 13 shows the dependence of trajectory pattern and travel time (to 2.5 m depth) on initial speed and orientation of the Rockan mine.

**Table 8 Examples of data for Rockan mines for a given initial velocity (2.805 m/s)**

| Time (s) | $x_1$ (m) | $y_1$ (m) | $z_1$ (m) | $x_2$ (m) | $y_2$ (m) | $z_2$ (m) |
|---|---|---|---|---|---|---|
| 0 | −1.0736 | 0.5296 | −5.166 | 1.0736 | −0.5296 | 5.166 |
| 0.016 | −2.5339 | −0.2221 | −10.5596 | 6.8934 | 0.0791 | −0.5933 |
| 0.032 | −4.0965 | −0.3357 | −12.7208 | 6.3428 | −0.4706 | −5.2315 |
| 0.048 | −6.2738 | −0.6902 | −14.0711 | 6.3564 | −1.1554 | −10.9224 |
| 0.064 | −7.6373 | −0.3879 | −13.5692 | 6.2505 | −1.0931 | −15.9247 |
| 0.08 | −8.1222 | −1.6365 | −15.0956 | 2.8875 | −0.9055 | −19.5188 |
| 0.096 | −7.7679 | −1.6508 | −15.1855 | 2.2667 | −0.6023 | −21.3069 |
| 0.112 | −6.2722 | −4.0571 | −22.3109 | 0.1216 | 3.0952 | −13.9761 |
| 0.128 | −4.3282 | −5.2784 | −24.7814 | −1.2973 | 2.809 | −17.453 |
| 0.144 | −3.2107 | −5.5892 | −26.6419 | −2.2431 | 3.5264 | −18.2012 |
| 0.16 | −1.1347 | −5.8973 | −28.332 | −3.0412 | 3.1642 | −19.8524 |
| 0.176 | −2.7208 | −5.1987 | −30.0086 | −3.3042 | 3.4589 | −23.1696 |
| 0.192 | −2.4592 | −5.3611 | −32.0709 | −3.1931 | 3.3691 | −24.8109 |
| 0.208 | −2.4199 | −5.7808 | −34.2118 | −3.2777 | 3.3184 | −26.3442 |
| 0.224 | −1.7248 | −6.6254 | −36.7567 | −2.9388 | 3.0883 | −27.4964 |
| 0.24 | −1.8801 | −6.1255 | −36.9698 | −3.2004 | 2.8093 | −30.25 |
| … | … | … | … | … | … | … |

**Table 9 Center of mass location ($x, y, z$) and orientation ($\psi_2, \psi_3$) for model Rockan mine derived from the data shown in Table 8**

| Time (s) | $x$ (m) | $y$ (m) | $z$ (m) | $\pi/2-\psi_2$ | $\psi_3$ |
|---|---|---|---|---|---|
| 0 | 0 | 0 | 0 | −1.3431 | −0.4583 |
| 0.016 | 2.1797 | −0.0715 | −5.5765 | −0.8129 | 0.0319 |
| 0.032 | 1.1232 | −0.4032 | −8.9761 | −0.6223 | −0.0129 |
| 0.048 | 0.0413 | −0.9228 | −12.4968 | −0.2442 | −0.0368 |
| 0.064 | −0.6934 | −0.7405 | −14.747 | 0.1678 | −0.0507 |
| 0.08 | −2.6173 | −1.271 | −17.3072 | 0.3813 | 0.0663 |
| 0.096 | −2.7506 | −1.1265 | −18.2462 | 0.5453 | 0.1041 |
| 0.112 | −3.0753 | −0.4809 | −18.1435 | −0.7153 | 0.8413 |
| 0.128 | −2.8128 | −1.2347 | −21.1172 | −0.7036 | 1.2122 |
| 0.144 | −2.7269 | −1.0314 | −22.4216 | −0.7442 | 1.4651 |
| 0.16 | −2.0879 | −1.3665 | −24.0922 | −0.7414 | 1.7782 |
| 0.176 | −3.0125 | −0.8699 | −26.5891 | −0.6675 | 1.6381 |
| 0.192 | −2.8262 | −0.996 | −28.4409 | −0.692 | 1.6547 |
| 0.208 | −2.8488 | −1.2312 | −30.278 | −0.7108 | 1.6648 |
| 0.224 | −2.3318 | −1.7686 | −32.1265 | −0.7576 | 1.6951 |
| 0.24 | −2.5402 | −1.6581 | −33.6099 | −0.6397 | 1.7175 |
| … | … | … | … | … | … |

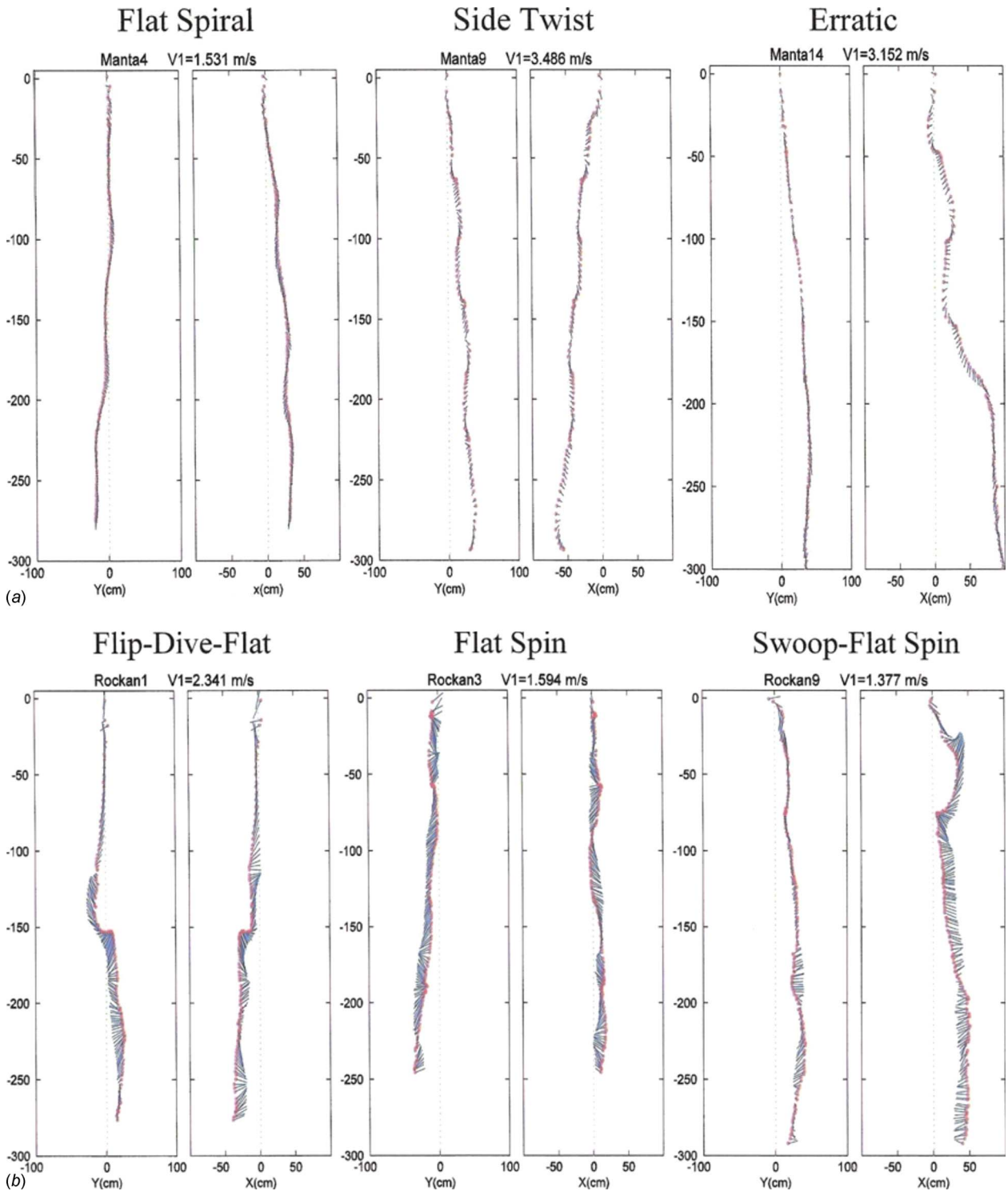


**Fig. 22 Trajectory patterns of model mines during MIDEX-II: (*a*) Manta and (*b*) Rockan mines**

The Manta mine tends to either fall with side-twist (0.40 probability) or with flat-spiral pattern (0.40 probability), and occasionally to fall with erratic pattern (0.20 probability). The Rockan mine tends to either fall with swoop-flat-spin (0.50 probability) or flip-dive-flat (0.36 probability) pattern. Both trajectory types show the potential gliding. For two drops (0.14 probability), the Rockan mine goes directly into a flat spin (Table 14).

For comparable initial speeds, the mean travel time (to 2.5 m depth) of Manta mine (3.703 s) is over twice that of either the Sphere or Gumdrop mines. The mean initial speed of Manta mine

**Table 10 Trajectory patterns of the model Manta mine**

| | |
|---|---|
| Flat spiral | The mine falls with its bottom side basically parallel to the *X-Y* plane and following a spiraling path. |
| Side twist | The mine falls with its bottom side perpendicular to the *X-Y* plane with the top side turning about the bottom in an alternating clockwise and anticlockwise motion. |
| Erratic | The mine falls in a flipping combination of side and flat spiraling and twisting. |

**Table 11 Distribution of trajectory patterns for 15 drops of Manta mine**

| Drop | Initial speed (m/s) | Initial orientation | Travel time (s) to 2.5 m depth | Trajectory pattern |
|---|---|---|---|---|
| 1 | 1.819 | $+X$ | 3.360 | Side twist |
| 2 | 1.573 | $+X$ | 3.956 | Flat spiral |
| 3 | 2.160 | $+X$ | 3.248 | Side twist |
| 4 | 1.531 | $+X, -Y$ | 4.800 | Flat spiral |
| 5 | 3.116 | $\pm X, -Y$ | 4.040 | Flat spiral |
| 6 | 1.653 | — | 4.544 | Flat spiral |
| 7 | 1.881 | $-Y$ | 5.040 | Flat spiral |
| 8 | 1.670 | $+X$ | 4.656 | Flat spiral |
| 9 | 3.486 | $-X, +Y$ | 3.120 | Side twist |
| 10 | 2.265 | $-X, +Y$ | 2.940 | Side twist |
| 11 | 2.398 | $+X, +Y$ | 3.216 | Erratic |
| 12 | 2.114 | $-X, +Y$ | 2.816 | Side twist |
| 13 | 3.143 | $+Y$ | 2.928 | Side twist |
| 14 | 3.152 | $+X, +Y$ | 3.176 | Erratic |
| 15 | 3.199 | $-X, +Y$ | 3.712 | Erratic |
| Average | 2.344 | | 3.703 | |

(2.344 m/s) is around 11% faster than the Rockan mine (2.097 m/s). However, the mean travel time (to 2.5 m depth) of Manta mine (3.703 s) is 22% shorter than the Rockan mine (4.688 s).

**7.5 Scaling Effect.** Scaling mines down from the actual mines does introduce potential for altered trajectory based on changing the drag coefficient. For true scaling, the Reynolds number is identical for the full scale and the 1/6 scale model (such as in MIDEX-II). It can be then inferred that the kinematic viscosity is reduced by the scale factor. Since the mine would be falling in the same fluid medium (water), kinematic viscosity remains the same. Thus the speed of the falling mine determines how much drag the mine experiences to affect its trajectory. In MIDEX-II, falling speeds of noncylindrical mines were primarily in the laminar flow regime. In that regime, the drag coefficient could change with different Reynolds numbers, but the speeds were of sufficient magnitude that the drag coefficient remained in the 0.5–0.6 range, reducing the drag coefficient error. A small amount of the speeds was in the turbulent flow region, where the drag coefficient changes very little for different Reynolds numbers, minimizing the drag coefficient error there as well. So the scaled models provide a good representation of the full scale mine. The Rockan scale model did have a specific trajectory issue independent of its Reynolds number, however. Scaling the Rockan shape to 1/6 the actual size of the operational mine reduced its ability to "glide" through the water as easily as the true Rockan, affecting the "realism" of the Rockan shape trajectory.

**Table 12 Trajectory patterns of the model Rockan mine**

| | |
|---|---|
| Flip-dive-flat | The mine flips once, goes into a vertical dive, and settles into a slowly spinning horizontal orientation for the remainder of the drop. |
| Flat spin | The mine immediately settles into a slowly spinning horizontal orientation and remains so for the whole of the drop. |
| Swoop-flat spin | The mine makes a "U" swooping motion upon entering the water, after which it settles into a slowly spinning horizontal orientation for the remainder of the drop. |

**Table 13 Trajectory patterns for Rockan mine**

| Drop | Initial velocity (m/s) | Initial orientation | Travel time (s) to 2.5 m depth | Trajectory pattern |
|---|---|---|---|---|
| 1 | 2.341 | $-X$ | 4.048 | Flip-dive-flat |
| 2 | 2.805 | $+X, -Y$ | 3.984 | Flip-dive-flat |
| 3 | 1.594 | $-Y$ | 5.472 | Flat spin |
| 4 | 1.066 | $+X, -Y$ | 5.824 | Swoop-flat spin |
| 5 | 1.796 | $+X, -Y$ | 6.176 | Swoop-flat spin |
| 6 | 2.213 | $+Y$ | 4.848 | Flat spin |
| 7 | 2.597 | $-X, -Y$ | 4.912 | Flip-dive-flat |
| 8 | 2.652 | $-Y$ | 4.880 | Flip-dive-flat |
| 9 | 1.377 | $+X, +Y$ | 4.672 | Swoop-flat spin |
| 10 | 2.378 | $+X, +Y$ | 4.138 | Swoop-flat spin |
| 11 | 2.018 | $+X, +Y$ | 4.868 | Swoop-flat spin |
| 12 | 2.289 | $+X, +Y$ | 3.156 | Flip-dive-flat |
| 13 | 1.872 | $+X, +Y$ | 4.740 | Swoop-flat spin |
| 14 | 2.362 | $+Y$ | 3.912 | Swoop-flat spin |
| Average | 2.097 | | 4.688 | |

**Table 14 Probability of trajectory-pattern occurrence for all mine shapes**

| Shape type | Trajectory type | Probability |
|---|---|---|
| **Manta** | Flat spiral | 0.40 |
| (15 total drops) | Side twist | 0.40 |
| | Erratic | 0.20 |
| **Rockan** | Flip-dive-flat | 0.36 |
| (14 total drops) | Flat spin | 0.14 |
| | Swoop-flat spin | 0.50 |

**7.6 IMPACT35 for Operational Mine Shapes.** Following the procedure in model development of IMPACT35C, three coordinate systems are also used to model the falling operational mines through the air, water, and sediment phases (Fig. 23): earth-fixed coordinate ($E$-coordinate), main-axis following coordinate ($M$-coordinate), and force following coordinate ($F$-coordinate) systems. All the coordinate systems are three dimensional, orthogonal, and right-handed. The origin of $M$- and $F$-coordinates is located at the COM of each operational mine. IMPACT35 for operational mine is used to solve the six scalar equations (43) and (44) to obtain $(x, y, z, \omega_1, \omega_2, \omega_3)$. From the angular velocity $(\omega_1, \omega_2, \omega_3)$, the three angles determining the mine orientation $(\psi_1, \psi_2, \psi_3)$ can be obtained. To do so, we need first to derive formulas for calculating the hydrographic (drag/lift) forces and torques for the operational mines. Here, we take IMPACT35-Manta as an example for illustration.

*7.6.1 Geometric Features of Manta Mine*. Manta mine is a combination of frustum and flat cylinder (Fig. 24). The frustum has a minimum radius ($R_1$) and a maximum radius ($R_2$) with a height of $L_1$. The flat cylinder has a radius of $R_2$ with a height of $L_2$ ($L_2 \ll L_1$). Let

$$\eta \equiv \frac{R_2 - R_1}{R_1} \tag{69}$$

be a geometric parameter of the Manta mine. The volume of the Manta mine is calculated by

$$\Pi = \frac{\pi L}{3}(R_1^2 + R_1 R_2 + R_2^2) = \pi L R_1^2 \left(1 + \eta + \frac{\eta^2}{3}\right) \tag{70}$$

The distances from the center of the smaller side of the frustum ($\bigcirc$) to the COV ($l_v$) and the center of hydrodynamic forces (COF) ($l_f$) are calculated by (Fig. 24)

$$l_v = \frac{\displaystyle\int_0^{L_1} \pi[R(x)]^2 x\,dx + \pi R_2^2 L_2 \left(L_1 + \frac{L_2}{2}\right)}{L_1 \int_0^{L_1} \pi[R(x)]^2 dx + \pi R_2^2 L_2} = \frac{L}{2} + \sigma_v \tag{71}$$

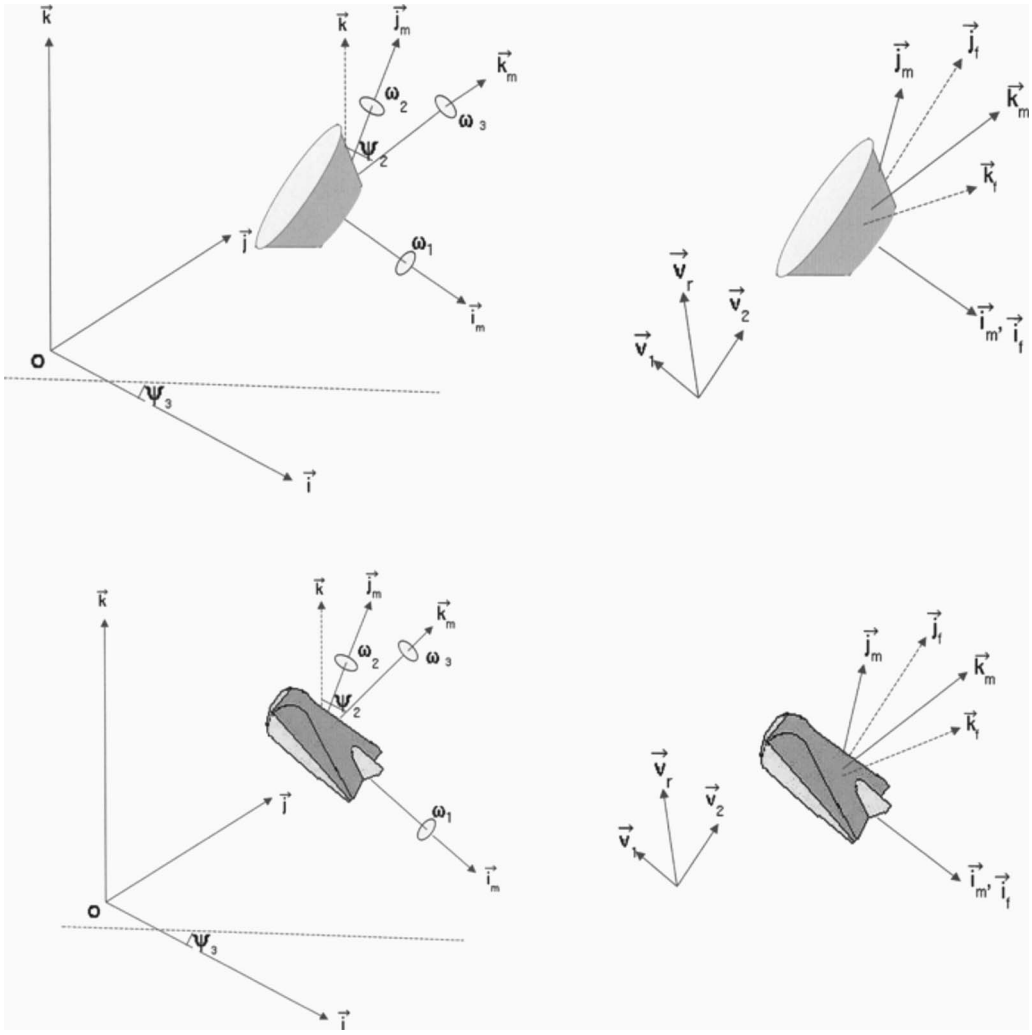

**Fig. 23 Three coordinate systems for Manta and Rockan shapes**

$$l_f = \frac{\int_0^{L_1} 2R(x)x\,dx + 2R_2L_2\left(L_1 + \frac{L_2}{2}\right)}{\int_0^{L_1} 2R(x)\,dx + 2R_2L_2} = \frac{L}{2} + \sigma_f \tag{72}$$

where

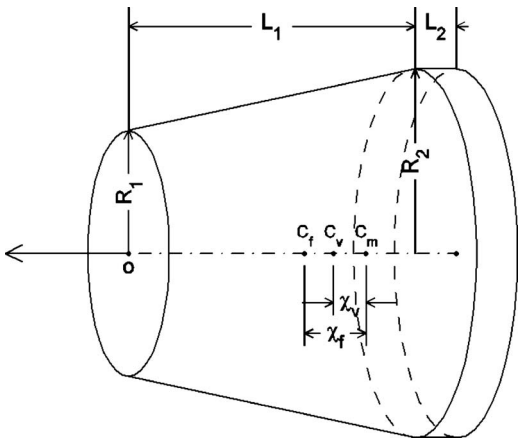

**Fig. 24 Location of $c_v$, $c_f$, and $c_m$. Here, $\chi_v$ is the distance between $c_v$ and $c_m$; $\chi_f$ is the distance between $c_f$ and $c_m$. Here, $R_1$ and $R_2$ are the small and large radii of the frustum.**

$$R(x) = R_1 + \frac{x}{L_1}(R_2 - R_1)$$

is the varying radius, $L=L_1+L_2$ is the total length of the frustum, and the two parameters $\sigma_v$ and $\sigma_f$ are defined by

$$\sigma_v \equiv \eta L \frac{\left(1 + \frac{\eta}{2}\right) + \frac{L_2}{L}\left(2 + \frac{3}{2}\eta\right)}{(6 + 6\eta + 2\eta^2) + 6\frac{L_2}{L_1}(1+\eta)^2},$$

$$\sigma_f = \eta L \frac{\left(1 + 2\frac{L_2}{L}\right)}{6(2+\eta) + 12(1+\eta)\frac{L_2}{L_1}} \tag{73}$$

The COF is the location where the resultant drag force exerts with the zero moment. Determination of the COF location is based on the assumption that the drag force exerts uniformly on the Manta mine surface. The distance between COM and COF is calculated by

$$\chi_f = \sigma_v - \sigma_f \tag{74}$$

Here $\chi_f$ is used to replace $\chi$ in Eqs. (56*a*), (56*b*), and (57) for calculating the drag/lift torques.

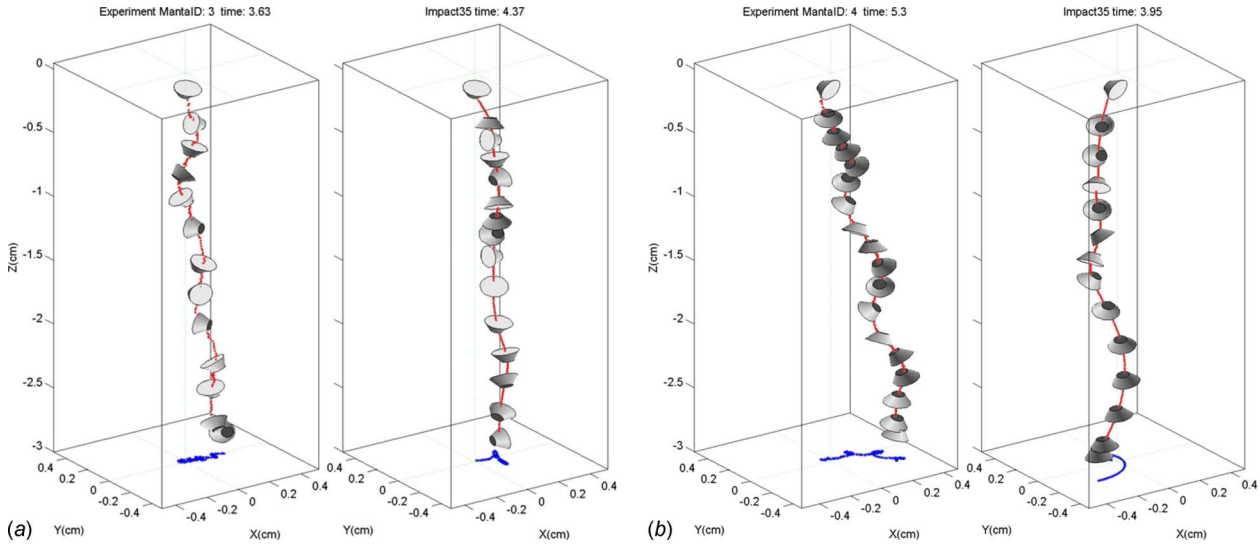


**Fig. 25 Model-data comparison of Manta mines maneuvering in water column**

*7.6.2 Drag/Lift Coefficients*. The Manta mine has large aspect ratio ($\delta=2R_2/L>1$). Similar to the cylindrical mines, the drag force is decomposed into along and cross axis components. The drag force along the main axis has two different types of calculation depending on the direction of the flow. When the water flows from $R_2$ to $R_1$, the Manta mine is treated as a disk with the radius ($R$) of $R_2$. When the water flows from $R_1$ to $R_2$, the Manta mine is treated as a disk with the radius ($R$) of $\sqrt{\Pi/(\pi L)}$, where $\Pi$ is the volume of the Manta mine. Thus, the Reynolds number (Re) is calculated using $\mathrm{Re}=2RU/\nu$.

Dependence of drag coefficient along the main axis ($C_{d1}$) on Reynolds number for a disk has been published as a curve using the experimental data by Crowe et al. [33]. From this curve, a semiempirical formula is derived to calculate the drag coefficient along the main axis,

$$C_{d1}=\begin{cases}1.5\left(\dfrac{105}{\mathrm{Re}}\right), & \mathrm{Re}<105\\ 1.5+0.3\left(\dfrac{\mathrm{Re}-105}{140-105}\right), & 105\le \mathrm{Re}<140\\ 1.8-(1.8-1.18)\left(\dfrac{\mathrm{Re}-140}{10^4-140}\right), & 140\le \mathrm{Re}<10^4\\ 1.18, & 10^4\le \mathrm{Re}\end{cases} \tag{75}$$

On the other hand the treatment of the drag force across the main axis and the lift force is relatively simpler since the obstacle of Manta mine to the flow is circular (the same as the cylinder). It is reasonable to use "equivalent cylinder" method, i.e., to compute the drag coefficient across the main axis ($C_{d2}$) and lift coefficient ($C_l$) using Eqs. (51) and (54) with the same volume ($\Pi$) and length ($L$) of the Manta mine as the equivalent cylinder.

*7.6.3 Moments of Inertia*. The moment of gyration tensor in the $M$-coordinate system for the Manta mine (i.e., a combined flustum and flat cylinder) is a diagonal matrix with the diagonal components (moments of inertia): $J_1$, $J_2$, and $J_3$,

$$J_1=\int_0^{L_1}\frac{\pi}{2}\rho R_1^4(1+x/L_1)^4dx+\frac{1}{2}\rho\pi R_2^4L_2$$

$$=\frac{\pi\rho L_1R_1^4(5+10\eta+10\eta^2+5\eta^3+\eta 4)}{10}+\frac{1}{2}\rho\pi R_2^4L_2$$

$$J_2=J_3=J_A+J_B \tag{76}$$

where $(J_A,J_B)$ are the inertias of the frustum and flat cylinder around COM. Let the distance between the center of the smaller side of the frustum ($\bigcirc$) to the COM be represented by $l_m$ (Fig. 24). The inertia components $(J_A,J_B)$ are calculated by

$$J_A=\int_0^{L_1}\frac{\pi\rho R_1^4}{4}(1+x/L_1)^4dx+\int_0^{L_1}\pi\rho R_1^2(1+x/L_1)^2(x-l_m)^2dx$$

$$=\frac{\pi\rho R_1^4L_1}{20}(5+10\eta+10\eta^2+5\eta^3+\eta^4)+\pi\rho R_1^2L_1^3\left(\frac{1}{3}-\frac{l_m}{L_1}+\frac{1}{2}\eta\right.$$

$$\left.-\frac{4}{3}\eta\frac{l_m}{L_1}+\eta\left(\frac{l_m}{L_1}\right)^2+\frac{\eta^2}{5}-\frac{\eta^2}{2}\left(\frac{l_m}{L_1}\right)+\frac{\eta^2}{3}\left(\frac{l_m}{L_1}\right)^2\right) \tag{77}$$

$$J_B=\frac{\pi\rho}{4}R_2^4L_2+\frac{\pi\rho}{12}R_2^2L_2^3+\pi\rho R_2^2L_2\left(L-\frac{L_2}{2}-l_m\right)^2 \tag{78}$$

*7.6.4 Model-Data Comparison*. The basic equations for IMPACT35-Manta are Eqs. (43) and (44) with the updated components $(J_1,J_2,J_3)$ (76) in the gyration tensor $\mathbf{J}$. The hydrodynamic force ($\mathbf{F}_h$) and torque ($\mathbf{M}_h$) are calculated using Eqs. (49), (50), (52), (53), (55), (56*a*), and (56*b*) using the updated drag coefficients $(C_{d1},C_{d2})$ and lift coefficient $C_l$ for the Manta mine. In the model development, the nonlinear instability and model sensitivity should be studied. Within the correct physics, there is a possibility of chaotic behavior in the model. The chaotic features will be handled by the instability and predictability analyses.

IMPACT35-Manta is integrated using the same Manta mine parameters and mine drop initial conditions (speed and orientation) as in the mine drop experiments (MIDEX-II, see Sec. 7.2). Performance of IMPACT35-Manta is verified through comparison between modeled and observed mine trajectories, travel times, and positions. The 3D model (IMPACT35-Manta) simulated trajectory agrees well with the observed trajectory (Fig. 25). Both show the same maneuvering pattern and the same travel time for the Manta mine passing through the water column. The modeled and observed vertical COM positions $[z^{\mathrm{mod}}(t),z^{\mathrm{obs}}(t)]$ are well compared for all the 15 drops in MIDEX-II (Fig. 25). Table 15 shows the comparison between IMPACT35-Manta and MIDEX-II (15 drops of Manta mine) on the mine maneuvering depth and corresponding travel time. The mean maneuvering depth predicted by the model is 2.947 m, which is very close to the observation

**Table 15 Verification of IMPACT35-Manta using MIDEX-II data**

| | Mean (MIDEX-II) | Mean (Model) | BIAS | RMSE |
|---|---|---|---|---|
| Travel time (s) | 4.425 | 4.175 | −0.25 | 0.9593 |
| Depth (m) | −2.942 | −2.947 | −0.005 | 0.0057 |

(2.942 m) (Fig. 26). The travel time predicted by the model is 4.175 s, which is a little faster than the observation (4.425 s).

## 8 Conclusions

Advances in the mine impact burial prediction in the past three decades are reviewed in this paper. The one-dimensional model (IBPM) was developed to predict the vertical position of the mine's COM. The model provides useful information such as higher falling velocity for vertical release than for horizontal release, strong dependence of water vertical impact velocity on the attitude for light mines (not for heavy mines), and strong dependence of the mine's falling velocity in water column on attitude, wet weight, mine's length, and mine's radius. For the same mine, the falling velocity in the water has a minimum in horizontal orientation and a maximum in vertical orientation. The major weakness is the constant falling angle assumption through a single fluid.

The two-dimensional model (IMPACT25/28) was developed to overcome the major weakness of the one-dimensional model and to predict the COM position in the $(x,z)$ plane and the rotation around the $y$-axis. The major weakness is the difficulty to include the fluid's motion into the model because it is impossible to lay a mine in the same direction of the fluid velocity. In littoral zone, the water velocity is not negligible. The application of the two-dimensional model for the operational use is limited. Other weaknesses include (a) a similar dependence of the axial and cross drag coefficients on the Reynolds number Re and the aspect ratio, and (b) crude parametrization for sediment bearing strength.

The three-dimensional model (IMPACT35) has been developed

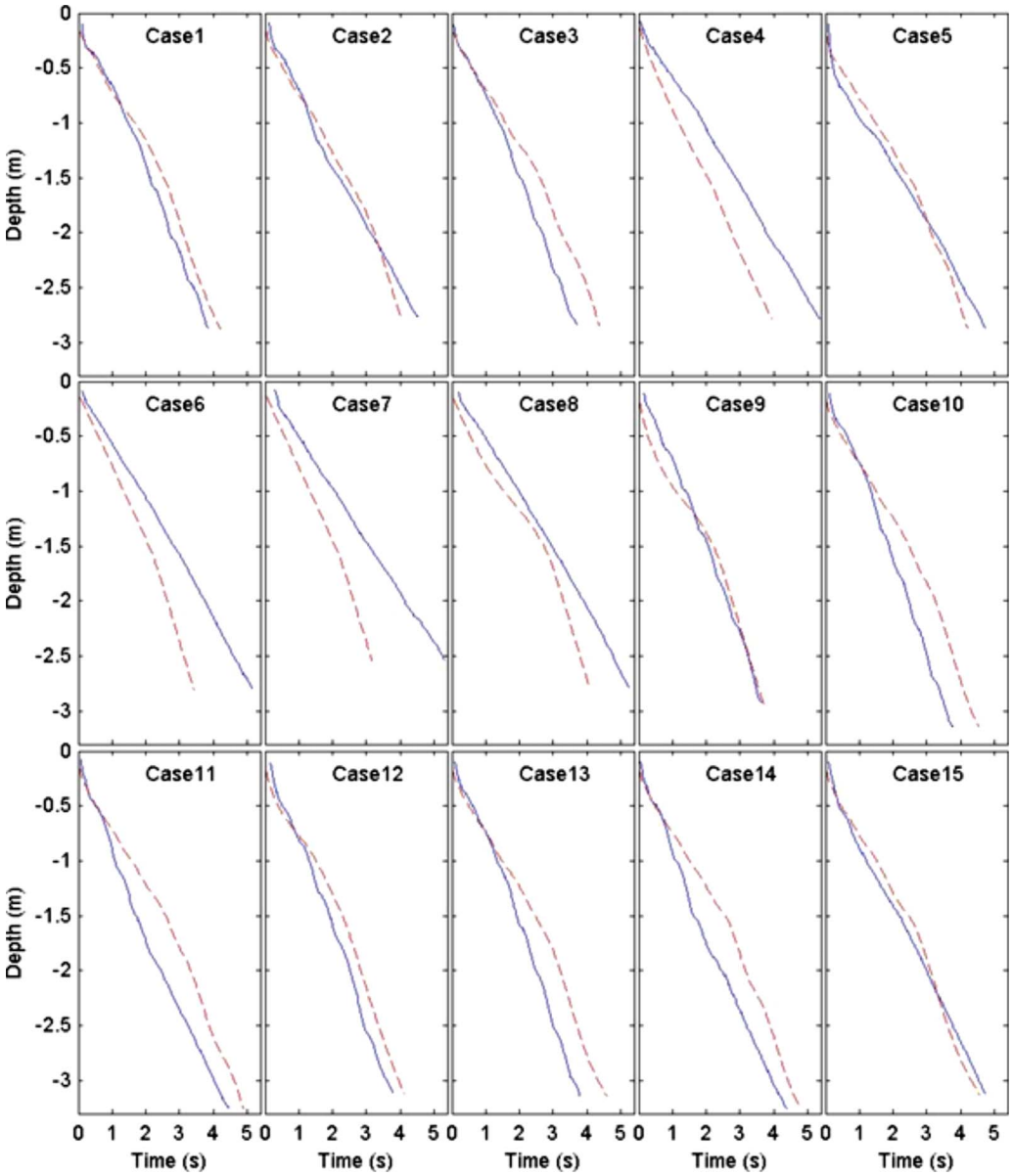


**Fig. 26 Model-data comparison of Manta mines maneuvering in water column. Here, the dashed curves represent model results, and the solid curves are observations.**

to predict the COM position in the $(x,y,z)$ space and the rotation around the $x$-, $y$-, and $z$-axes. IMPACT35 shows great improvements versus IMPACT25/28 using the recent mine drop experimental data. Furthermore, the mine shape effect is also included into the three-dimensional model (IMPACT35-Operational). The most important features of the Manta mine are well predicted when the modeled data are compared to the data collected during MIDEX-II at NPS for operational mine shapes such as Manta and Rockan. The drag and lift laws for noncylindrical mines are also derived.


## Acknowledgment

The Office of Naval Research Coastal Geosciences Program (N0001403WR20178, N0001404WR20067), the Naval Oceanographic Office, and the Naval Postgraduate School supported this study. The author was benefited from the discussion with Mr. Brian Almquist at the Office of Naval Research, RAML (retired) Rick Williams, Mr. Chenwu Fan at the Naval Postgraduate School, CAPT James Berdegues and CAPT Robert Kiser at the Commander Naval Meteorology and Oceanography Command (CNMOC), Mr. Ronald Betsch, Dr. Peter Fleischer, and Mr. Steven Haeger at the Naval Oceanographic Office, Dr. Phil Valent, Dr. Michael Richardson, Dr. Paul Elmore, Dr. Ted Holland, and Dr. Andrei Abelev at the Naval Research Laboratory at Stennis Space Center, and Dr. Thomas Weaver at the German Federal Armed Forces Underwater Acoustic and Marine Geophysics Research Institute. Comments from Professor Firdaus Udwadia at the University of Southern California and an anonymous reviewer are extremely useful for improvement of the manuscript.


## Nomenclature

$(C_{d1}, C_{d2})$ = drag coefficients along and across the cylinder
$C_l$ = lift coefficient
$C_{tl}$ = translational lift coefficient (kg s$^{-1}$)
$e_v$ = void ratio
$(f_1, f_2, f_3)$ = added-mass ratios for drag and lift forces
$f_r$ = added-mass ratio for moment of drag and lift forces
$(f_{rd2}, f_{rd3})$ = rotational drag force (N)
$\mathbf{F}_b$ = buoyancy force (N)
$\mathbf{F}_d$ = drag force (N)
$(\mathbf{F}_{d1}, \mathbf{F}_{d2}, \mathbf{F}_{d3})$ = drag force in the $F$-coordinate (N)
$\mathbf{F}_l$ = lift force (N)
$(\mathbf{F}_{l1}, \mathbf{F}_{l2}, \mathbf{F}_{l3})$ = lift force in the $F$-coordinate (N)
$(\mathbf{i}_E, \mathbf{j}_E, \mathbf{k}_E)$ = unit vectors in the $E$-coordinate
$(\mathbf{i}_F, \mathbf{j}_F, \mathbf{k}_F)$ = unit vectors in the $F$-coordinate
$(\mathbf{i}_M, \mathbf{j}_M, \mathbf{k}_M)$ = unit vectors in the $M$-coordinate
$(J_1, J_2, J_3)$ = moments of gyration (kg m$^2$)
$(J_1^{(i)}, J_2^{(i)}, J_3^{(i)})$ = moments of gyration for cylindrical part-$i$ (kg m$^2$)
$L$ = length of the cylinder (m)
$\mathbf{M}_b$ = torque due to the buoyancy force (kg m$^2$ s$^{-2}$)
$\mathbf{M}_h$ = torque due to the hydrodynamic force (kg m$^2$ s$^{-2}$)
$(\mathbf{M}_{d1}, \mathbf{M}_{d2}, \mathbf{M}_{d3})$ = torques due to the drag force in the $M$-coordinate (kg m s$^{-2}$)
$\mathbf{r}$ = position vector (in the $M$-coordinate) of point on the cylinder's surface
$R$ = radius of the cylinder
Re = Reynolds number
$\mathbf{V}$ = translation velocity (m s$^{-1}$)
$\mathbf{V}_r$ = water-to-cylinder velocity (m s$^{-1}$)
$\mathbf{V}_1$ = component of $\mathbf{V}_r$ along the cylinder (m s$^{-1}$)
$\mathbf{V}_2$ = component of $\mathbf{V}_r$ perpendicular to the cylinder (m s$^{-1}$)
$\mathbf{V}_w$ = water velocity (m s$^{-1}$)
$\Lambda$ = effective cross section area (m$^2$)
$\mu$ = dynamic viscosity of the water (m$^2$ s$^{-1}$)
$\nu$ = kinematic viscosity of the water (m$^2$ s$^{-1}$)
$\Pi$ = volume of the cylinder (m$^3$)
$\rho$ = density of the cylinder (kg m$^{-3}$)
$\rho_w$ = density of the water (kg m$^{-3}$)
$\chi$ = distance between COM and COV (m) in cylindrical mines
$\chi_f$ = distance between COM and COF (m) in noncylindrical mines
$\chi_v$ = distance between COM and COV (m) in noncylindrical mines
$(\psi_1, \psi_2, \psi_3)$ = angles determining the cylinders' orientation
$\boldsymbol{\omega}$ = angular velocity (s$^{-1}$)
$(\omega_1, \omega_2, \omega_3)$ = angular velocity components in the $M$-coordinate (s$^{-1}$)
$(\omega_1^F, \omega_2^F, \omega_3^F)$ = angular velocity components in the $F$-coordinate (s$^{-1}$)

## References


[1] Arnone, R. A., and Bowen, L. E., 1980, "Prediction Model of the Time History Penetration of a Cylinder Through the Air-Water-Sediment Phases," Naval Coastal Systems Center, NCSC Technical Note 734-36.
[2] Satkowiak, L. J., 1987, "Modifications to the NCSC Impact Burial Prediction Model," Naval Coastal Systems Center, NCSC Technical Note 883-87.
[3] Satkowiak, L. J., 1987, "User's Guide for the Modified Impact Burial Prediction Model," Naval Coastal Systems Center, NCSC TN 884-87.
[4] Hurst, R. B., 1992, "Mine Impact Burial Prediction Model-Technical Description of Recent Changes and Developments (U)," (Restricted), Defense Scientific Establishment, DSE Report 149.
[5] Mulhearn, P. J., 1992, "Experiments on Mine Burial on Impact-Sydney Harbour," U.S. Navy Journal of Underwater Acoustics, **43**, pp. 1271–1281.
[6] Chu, P. C., Gilles, A. F., Fan, C. W., and Fleischer, P., 2000, "Hydrodynamics of Falling Mine in Water Column," *Proceedings of the Fourth International Symposium on Technology and the Mine Problem*, Naval Postgraduate School, Monterey, CA, p. 10.
[7] Chu, P. C., Taber, V. L., and Haeger, S. D., 2000, "Environmental Sensitivity Studies on Mine Impact Burial Prediction Model (Two-Dimensional)," *Proceedings of the Fourth International Symposium on Technology and the Mine Problem*, p. 10.
[8] Taber, V. L., 1999, "Environmental Sensitivity Studies on Mine Impact Burial Prediction Model," Master thesis, Naval Postgraduate School, Monterey.
[9] Smith, T. B., 2000, "Validation of the Mine Impact Burial Model Using Experimental Data," Master thesis, Naval Postgraduate School, Monterey.
[10] Chu, P. C., Evans, A. D., Gilles, A. F., Smith, T., and Taber, V., 2004, "Development of Navy's 3D Mine Impact Burial Prediction Model (IMPACT35)," *Proceedings of the Sixth International Symposium on Technology and the Mine Problem*, Naval Postgraduate School, Monterey, CA, p. 10.
[11] Chu, P. C., and Fan, C. W., 2007, "Mine Impact Burial Model (IMPACT35) Verification and Improvement Using Sediment Bearing Factor Method," IEEE J. Ocean. Eng., **32**(1), pp. 34–48.
[12] Chu, P. C., 2002, "Hydrodynamics of Mine Impact Burial," ONR Impact Burial Annual Workshop, La Jolla, CA, Jan. 15–17.
[13] Chu, P. C., Fan, C. W., Evans, A. D., Gilles, A. F., and Fleischer, P., 2003, "Three-Dimensional Hydrodynamic Model for Prediction of Falling Cylinder Through Water Column," *The OCEANS 2003 MTS/IEEE Conference Proceedings*, San Diego, CA, p. 10.
[14] Chu, P. C., Fan, C. W., and Evans, A. D., 2004, "Three-Dimensional Rigid Body Impact Burial Model (IMPACT35)," Advances in Fluid Mechanics, **5**, pp. 43–52.
[15] Evans, A. D., 2002, "Hydrodynamics of Mine Impact Burial," Master thesis, Naval Postgraduate School, Monterey.
[16] Chu, P. C., Fan, C. W., Evans, A. D., and Gilles, A. F., 2004, "Triple Coordinate Transforms for Prediction of Falling Cylinder Through the Water Column," ASME J. Appl. Mech., **71**, pp. 292–298.
[17] Lamb, H., 1932, *Hydrodynamics*, Cambridge University Press, ASME, Cambridge.
[18] Milne-Thomson, L. M., 1968, *Theoretical Hydrodynamics*, Macmillan, New York.
[19] Aref, H., and Jones, S. W., 1993, "Chaotic Motion of a Solid Through Ideal Fluid," Phys. Fluids A, **5**(12), pp. 3026–3028.

[20] Aref, H., and Jones, S. W., 1994, "Motion of a Solid Body Through an Ideal Fluid," College of Engineering, University of Illinois at Urbana-Champaign, Report No. 772.
[21] Holmes, P., Jenkins, J., and Leonard, N. E., 1998, "Dynamics of the Kirchhoff Equations I: Coincident Centers of Gravity and Buoyancy," Physica D, **118**(3–4), pp. 311–342.
[22] Field, S. B., Klaus, M., Moore, M. G., and Nori, F., 1997, "Chaotic Dynamics of Falling Disks," Nature (London), **388**(6639), pp. 252–254.
[23] Mahadevan, L., Ryu, W. S., and Aravinthan, D. T. S., 1999, "Tumbling Cards," Phys. Fluids, **11**(1), 1–3.
[24] Kochin, N. E., Kibel, I. A., Roze, N. V., 1964, *Theoretical Hydromechanics*, Intersciences, New York.
[25] Kozlov, V. V., 1989, "Heavy Rigid Body Falling in an Ideal Fluid," Izv AN SSSR, Mekhanika Tverdogo Tela, **24**(5), pp. 10–17.
[26] Satkowiak, L. J., 1988, "Modified NCSC Impact Burial Prediction Model with Comparisons to Mine Drop Tests," Naval Coastal Systems Center, NCSC TN 486-88.
[27] Chu, P. C., 2002, "Ensemble Mine Impact Burial Prediction," ONR Impact Burial Modeling Workshop, Phoenix, AZ, March 5–7.
[28] Chu, P. C., Taber, V. L., and Haeger, S. D., 2000, "A Mine Impact Burial Model Sensitivity Study," Naval Postgraduate School, NPS-IJWA-00-003.
[29] Stanley, E. M., 1969, "Viscosity of Sea Water at Moderate Temperatures and Pressures," J. Geophys. Res., **74**, 3415–3420.
[30] Krone, R. B., "A Study of Rheological Properties of Estuarine Sediments," Technical Bulletin No. 7.
[31] Chu, P. C., Smith, T. B., and Haeger, S. D., 2001, "Mine Impact Burial Prediction Experiment," Naval Postgraduate School, NPS-IJWA-01-007.
[32] Chu, P. C., Smith, T. B., and Haeger, S. D., 2002, "Mine Impact Burial Prediction," *Proceedings of the Fourth International Symposium on Technology and the Mine Problem*, Naval Postgraduate School, Monterey, CA, p. 10.
[33] Crowe, C. T., Roberson, J. A., and Elger, D. F., 2001, "Engineering Fluid Mechanics," 7th ed., Wiley, New York, pp. 1–714.
[34] Chu, P. C., Gilles, A. F., Fan, C. W., Lan, J., and Fleischer, P., 2002, "Hydrodynamics of Falling Cylinder in Water Column," Advances in Fluid Mechanics, **4**, pp. 163–181.
[35] Chu, P. C., and Fan, C. W., 2005, "Pseudo-Cylinder Parameterization for Mine Impact Burial Prediction," ASME J. Fluids Eng., **127**, pp. 1515–1520.
[36] Chu, P. C., and Fan, C. W., 2006, "Prediction of Falling Cylinder Through Air-Water-Sediment Columns," ASME J. Appl. Mech., **73**, pp. 300–314.
[37] Chu, P. C., and Ray, G., 2006, "Prediction of High Speed Rigid Body Maneuvering in Air-Water-Sediment Column," Advances in Fluid Mechanics, **6**, pp. 123–132.
[38] Chu, P. C., Ray, G., Fleischer, P., and Gefken, P., 2006, "Development of Three Dimensional Bomb Maneuvering Model," *Proceedings of the Seventh Monterey International Symposium on Technology and Mine Problems*, Naval Postgraduate School, Monterey, CA, p. 10.
[39] Rouse, H., 2006, *Fluid Mechanics for Hydraulic Engineers*, 1st ed., McGraw-Hill Book, New York, p. 422.
[40] Von Mises, R., 1959, *Theory of Flight*, Dover, New York, pp. 564–585.
[41] Sumer, B. M., and Fredsøe, J., 1997, *Hydrodynamics Around Cylindrical Structures*, World Scientific, Singapore, p. 530.
[42] White, F. M., 1974, *Viscous Fluid Flow*, McGraw-Hill Inc., New York, p. 712.
[43] Hansen, N. E. O., Simonsen, B. C., and Sterndoff, M. J., 1994, "Soil Mechanics of Ship Beaching," *Proceedings of 24th International Conference on Coastal Engineering*, Kobe, Japan, p. 3030–3044.
[44] Aubeny, C. P., and Shi, H., 2007, "Effect of Rate-Dependent Soil Strength on Cylinders Penetrating Into Soft Clay," IEEE J. Ocean. Eng., **32**(1), pp. 49–56.
[45] Gilles, A. F., 2001, "Mine Drop Experiment," Master thesis, Naval Postgraduate School, Monterey.
[46] Chu, P. C., Gilles, A. F., and Fan, C. W., 2005, "Experiment of Falling Cylinder Through the Water Column," Exp. Therm. Fluid Sci., **29**, pp. 555–568.
[47] Abelev, A. V., Valent, P. J., and Holland, K. T., 2007, "Behavior of a Large Cylinder in Free Fall Through Water," IEEE J. Ocean. Eng., **32**(1), pp. 10–20.
[48] Holland, K. T., Green, A. W., Abelev, A., and Valent, P. J., 2004, "Parameterization of the In-Water Motions of Falling Cylinders Using High-Speed Video," Exp. Therm. Fluid Sci., **37**, pp. 690–770.
[49] Elmore, P. A., Wilkens, R., Weaver, T., and Richardson, M. D., 2005, "IMPACT 28 and 35 Simulations of 2003 Baltic Sea Cruise: Model Results and Comparison with Data," Fifth Annual ONR Workshop on Mine Burial Prediction, Kona, HI, Jan. 31–Feb. 2.
[50] Elmore, P. A., Richardson, M. D., and Wilkens, R. H., 2007, "Exercising a Deterministic Mine Burial Prediction System for Impact and Scour Burial for Operational Navy Use," IEEE J. Ocean. Eng., **32**(1), pp. 273–283.
[51] Chu, P. C., Allen, C. R., and Fleischer, P., 2006, "Non-Cylindrical Mine Impact Experiment," *Proceedings of the Seventh Monterey International Symposium on Technology and Mine Problems*, Naval Postgraduate School, Monterey, CA, p. 10.
[52] Allen, C. R., 2006, "Mine Drop Experiment II with Operational Mine Shapes (MIDEX-II)," Master thesis, Naval Postgraduate School, Monterey.

**Dr. Peter Chu** *is a Professor of Oceanography and head of the Naval Ocean Analysis and Prediction (NOAP) Laboratory at the Naval Postgraduate School. His research interests include ocean analysis and prediction, coastal modeling, littoral zone oceanography for mine warfare, mine impact burial prediction, mine acoustic detection, and satellite data assimilation for undersea warfare. He received his Ph.D. in Geophysical Fluid Dynamics from the University of Chicago in 1985.*